DOI 10.1002/2015GC006019

Coupling changes in densities and porosity to fluid pressure variations in reactive porous fluid flow. Local thermodynamic equilibrium.

Benjamin Malvoisin[1, 2], Yury Yu. Podladchikov[2], and Johannes C. Vrijmoed [3]

[1]Centre d'Hydrogéologie et de Géothermie, Université de Neuchâtel, Neuchâtel, Switzerland.

[2]Institut des Sciences de la Terre, Université de Lausanne, Lausanne, Switzerland.

[3]Inst. f. Geochemie und Petrologie, ETH Zurich, Switzerland

Corresponding author: B. Malvoisin, Centre d'hydrogéologie et de Géothermie, Université de Neuchâtel, Rue Emile Argand CH 2000 Neuchâtel, Switzerland. (benjamin.malvoisin@unine.ch)

Abstract

Mineralogical reactions which generate or consume fluids play a key role during fluid flow in porous media. Such reactions are linked to changes in density, porosity, permeability and fluid pressure which influence fluid flow and rock deformation. To understand such a coupled system equations were derived from mass conservation and local thermodynamic equilibrium. The presented mass conservative modelling approach describes the relationships between evolving fluid pressure, porosity, fluid and solid density, and devolatilization reactions in multi-component systems with solid solutions. This first step serves as a framework for future models including aqueous speciation and transport. The complexity of univariant and multi-variant reactions is treated by calculating look-up tables from thermodynamic equilibrium calculations. Simplified cases were also investigated to understand previously studied formulations. For non-deforming systems or systems divided into phases of constant density the equations can be reduced to porosity wave equations with addition of a reactive term taking the volume change of reaction into account. For closed systems an expression for the volume change of reaction and the associated pressure increase can be obtained. The key equations were solved numerically for the case of devolatilization of three different rock types that may enter a subduction zone. Reactions with positive Clapeyron slope lead to increase in porosity and permeability with decreasing fluid pressure resulting in sharp fluid pressure gradients around a negative pressure anomaly. The opposite trend is obtained for reactions having a negative Clapeyron slope during which sharp fluid pressure gradients were only generated around a positive pressure anomaly. Coupling of reaction with elastic deformation induces a more efficient fluid flow for reactions with negative Clapeyron slope than for reactions with positive Clapeyron slope.

1 Introduction

Fluids in the Earth's lithosphere enhance mineral reaction and melting, facilitate mass transport and change bulk physical rock properties such as density and rheology. Therefore a variety of formulation and numerical models have been developed to simulate reactive transport in a porous medium from the micro to

Received: Jul 17, 2015; Revised: Oct 28, 2015; Accepted: Nov 16, 2015

the kilometer scale with applications to fundamental geological processes (*e.g.* metamorphic reactions) as well as to societal problems (*e.g.* CO_2 capture and storage) [*Steefel et al.*, 2005].

Provided that an interconnected network of pores exists that results in sufficiently permeable rock, fluid will flow due to gradients in fluid pressure. The generation of fluid pressure gradients and porosity variations may result from rock deformation (such as compaction), it may be a result of volume change during chemical reactions or volume changes due to thermal processes for example in contact aureoles [e.g. *Connolly*, 1997; *Aarnes et al.*, 2012; *Putnis and Putnis*, 2007].

For metamorphic reactions a series of local equilibrium models developed starting with the work of *Korzhinskii* [1970] and *Thompson* [1970]. These models were dealing mainly with mass transport of elements by diffusion and advection due to fluid flow and the development of metasomatic zones. *Hofmann* [1972] exploited the chromatographic theory for infiltration metasomatism to show how sharp fronts developed due to the particular shape of the relation between solid concentration and fluid concentration (called the isotherm), with application to feldspar. The model used assumptions of constant small porosity and isobaric conditions. *Frantz and Mao* [1976] developed a metasomatic model which could be used to quantify the widths and growth speeds of metasomatic reaction zones. They showed that in case the system is characterized by steady state concentration gradients, these could be used to predict zone width and growth speed. To arrive at this they assumed that porosity was constant and small, so that change of concentration is mainly due to change in the solid concentration due to reaction. Additionally, they assumed growth of zones took place at constant pressure. *Guy* [1993] and *Sedqui and Guy* [2001] revised the Korzhinskii's theory of metasomatism with a more rigorous mathematical treatment identifying the development of metasomatic zones either as sharp shock waves or as spreading waves. An essential feature of these metasomatic

models is the prediction of sharp metasomatic fronts due to the mass transport of major elements and local equilibrium assumptions between fluid and solid. The chromatographic theory was also successfully used for understanding trace element partitioning between melt and rock [*Navon and Stolper*, 1987]. At the regional scale, mass transport was quantitatively constrained by *Baumgartner and Ferry* [1991] who derived an equation for determining the direction and the amount of fluid fluxes during metamorphism.

Major progress has been made in reactive transport modelling motivated by the need to predict subsurface contamination and evaluate safety of nuclear waste disposal [*Lichtner et al.*, 1987; *Lichtner and Carey*, 2006; *Lichtner and Kang*, 2007; *Xu et al.*, 2006]. These models included chemical reactions and kinetics, porosity evolution caused by volume changes during reaction, advective and diffusive transport, whereas they did not treat the mechanics of rock deformation. However, reaction-induced deformations have been shown to modify the hydraulic properties by generating fluid pathways such as fractures [*Fletcher and Merino*, 2001; *Scherer*, 2004; *Jamtveit et al.*, 2009; *Plümper et al.*, 2012].

Purely mechanical models with more complex rheology have been developed to model dynamic porosity and fluid flow in compacting rocks [*McKenzie*, 1984; *Connolly and Podladchikov*, 1998, 2007, 2013, 2015; *Connolly*, 2010; *Keller et al.*, 2013]. These models take into account the compressibility of solid and fluid and show the development of solitary porosity waves due to buoyancy effects. Although these models do not consider chemical reactions progress has been made in understanding blob-like porosity waves [*Wiggins and Spiegelman*, 1995] versus channel-shaped porosity perturbations [*Connolly and Podladchikov*, 1998].

Connolly [1997] developed a numerical model coupling devolatilization reactions with mechanical compaction and heat flow. The model predicts the porosity and

fluid pressure evolution initiated by a devolatilization reaction which in turn are coupled through temperature by ΔG. Similarly, *Balashov and Yardley* [1998] proposed a model to simulate fluid flow coupled to mechanical compaction and volume change of reactions. *Spiegelman et al.* [2001], *Hesse et al.* [2011] and *Liang et al.* [2011] also consider the influence of reaction on deformation to investigate magma generation at mid-ocean ridges. In these models, the authors selected reactions which are the most representative of the system and used a kinetic law with a dependence on the distance from the equilibrium to estimate the rate of fluid release from the rock. Recently, *Wilson et al.* [2014] used a purely thermodynamic approach with pseudosections to estimate the amount of fluid released from a slab when progressing in the P-T space during subduction. This amount was then used to predict porosity and compaction pressure changes due to reactions.

In addition to the aforementioned assumptions of constant porosity in some models, lack of chemical reactions in others, assumption of preexisting background porosity, in most of the reactive fluid-flow models the density of the solid is assumed to be constant [*Katz et al.*, 2007]. However, it is known to vary by more than 30 % in subduction zones due to dehydration reactions [*Hacker*, 2003]. This dehydration-induced densification is known to have consequences on geodynamics and numerical models with compressible rocks have to be developed [*Hetényi et al.*, 2011; *Hetényi*, 2014].

Fluid pressure variations induced by volume changes of reaction can influence the extent of reaction [e.g. *Aarnes et al.*, 2012]. Some models have already included these effects [*Connolly*, 1997] whereas others have used simplications such as using lithostatic pressure to compute stable phase assemblage in each local equilibrium domain [*Duesterhoeft et al.*, 2014; *Tirone et al.*, 2009]. As already theoretically demonstrated by *Bruton and Helgeson* [1983], used by *Dahlen* [1992] and confirmed by field data [*Holdaway and Goodge*, 1990] and experiments [*Llana-Fúnez et al.*, 2012], it is the fluid pressure that determines

stable phases and composition in each local equilibrium domain. Therefore a consistent treatment of the thermodynamic part of the model requires the use of the fluid pressure.

Here, we present the theoretical development of a reactive-fluid flow modelling approach founded on mass conservation and local thermodynamic equilibrium. The new approach (1) treats dynamic porosity and evolution of densities due to reactions and deformation; (2) includes full compressibility of rock, minerals, and fluid; (3) uses variable fluid pressure in calculating local equilibrium. Reactions are computed based on Gibbs minimization allowing for any possible reaction and includes solid solutions. The focus here is on coupling changes in densities and porosity to evolution of fluid pressure for devolatilization reactions at constant temperature and system composition. The main coupling effect in this reactive fluid flow approach is achieved through fluid pressure which controls the local reactions by its evolution during flow. In general, solid components may dissolve as aqueous species into the fluid and be transported by diffusion and advection in the fluid. This transport is not considered here since dissolved solid components generally represent a small proportion of the total system. Current progress in modelling aqueous fluid speciation for metamorphic rocks suggests that small concentrations of components in the fluid do not significantly alter the phase diagrams [*Galvez et al.*, 2015]. This fact suggests a two stage approach for the local thermodynamic equilibrium calculations. First, compute the equilibrium assemblage of solid phases and their chemical potentials in equilibrium with pure fluid. Second, compute the aqueous species in equilibrium with solids obtained in the first step (see [*Galvez et al.*, 2015] for more details). Only the first step is considered in this contribution. Therefore only the main effect of reactions on density, fluid pressure, and porosity changes is captured by the approach presented here without considering transport of dissolved solids in the fluid. Even if solubilities of the solids in a fluid is small, maintenance of high fluid flux over extended periods of time can lead to significant change in the local bulk composition, that may significantly change the local reactions. Although not

taken into account here the approach is extendable to include element partitioning between fluid and solid, bulk rock compositional changes by diffusion and advection, and temperature changes. Any of these extensions would require extensive benchmarking of the first step coupling thermodynamic calculations that predict solids in equilibrium with pure fluid to the fluid flow and deformation. In the following, the derivation of the equations is presented and explored using simplifying assumptions. It is demonstrated that the derived equations are numerically solvable. A solution to the system of equations for chemical systems with different properties can be generally non-intuitive. Therefore the main aim is to simply present the solution for three different rock types with different Clapeyron slopes. This will then provide the basis to improve the understanding of the physics of the models and can be used as initial benchmarks for more complex models.

2 Model formulation

In this contribution, we consider time scales long enough to establish local thermodynamic equilibrium and thermal equilibration at scales ranging from microscopic to typical outcrop dimensions.

2.1 Mass conservation

During deep crustal metamorphism or near-surface alteration, fluids can be incorporated or released from the rock during the formation or the breakdown of volatile-bearing minerals. Aqueous species in the fluid are not considered here and neither are diffusion and advection of components in fluid and solid. Therefore, both the total amount of volatile species (as free fluid and as volatile species bound to minerals) and the total amount of non-volatile species (such as Si, Mg, Al, Fe) are conserved. Mass conservation of the total system is expressed as:

$$\frac{\partial\left(\rho_f\phi+\rho_s\left(1-\phi\right)\right)}{\partial t}+\nabla\cdot\left(\rho_f\phi\overrightarrow{v_f}+\rho_s\left(1-\phi\right)\overrightarrow{v_s}\right)=0 \qquad (1)$$

where ϕ, ρ, $\vec{v}$ are the porosity (volume fraction of fluid), the density and the velocity, respectively. Subscripts *f* for fluid and *s* for solid are used where needed. An overview of all notations is given in Table 1.

Mass of the non-volatile species is conserved as well:

$$\frac{\partial\left(\rho_s\left(1-X_s\right)\left(1-\phi\right)\right)}{\partial t}+\nabla\cdot\left(\rho_s\left(1-X_s\right)\left(1-\phi\right)\overrightarrow{v_s}\right)=0 \quad (2)$$

where X_s is the mass fraction of fluid in solid.

Equations (1) and (2) can be re-arranged (see Appendix A) by replacing partial time derivatives by material derivatives ($\frac{d}{dt}=\frac{\partial}{\partial t}+\overrightarrow{v_s}\cdot\nabla$ and $\frac{d_t}{dt}=\frac{\partial}{\partial t}+\left(\phi\overrightarrow{v_f}+\left(1-\phi\right)\overrightarrow{v_s}\right)\cdot\nabla$):

$$\frac{\left(1-\phi\right)\rho_n}{\rho_f}\frac{dR}{dt}+\frac{d_t\log\rho_f}{dt}+\nabla\cdot\overrightarrow{v_s}+\nabla\cdot\phi\left(\overrightarrow{v_f}-\overrightarrow{v_s}\right)=0 \quad (3)$$

$$\frac{1}{\left(1-\phi\right)}\frac{d\phi}{dt}=\frac{d\log\rho_n}{dt}+\nabla\cdot\overrightarrow{v_s} \quad (4)$$

where two shorthand notations have been introduced for two thermodynamically constrained quantities, the density of the non-volatile species:

$$\rho_n=\rho_s\left(1-X_s\right) \quad (5)$$

and the density ratio:

$$R=\frac{\rho_s-\rho_f}{\rho_n} \quad (6)$$

In Equations (3) and (4), fluid flux and solid deformation are related to thermodynamic changes. These changes are due to two contributions: fluid and

the solid compressibilities, and reactions which modify fluid and solid densities, porosity and the amount of chemically bound fluid in the solid.

2.2 Conservation of momentum

Conservation of fluid momentum is expressed by the Darcy's law:

$$\phi\left(\vec{v_f} - \vec{v_s}\right) = -\frac{k_0\phi^3}{\mu_f}\left(\nabla P_f + \rho_f g \vec{e_z}\right) \quad (7)$$

where the permeability is related to the porosity through a constant background permeability, k_0, times the porosity to the exponent 3, μ_f is the fluid viscosity and P_f the fluid pressure.

Conservation of total momentum (porous solid and fluid) assuming negligible shear stresses is given by:

$$\nabla \overline{P} = -(\phi\rho_f + (1-\phi)\rho_s) g \vec{e_z} \quad (8)$$

with $\overline{P}$ the total pressure.

2.3 Rheology

In the following, we use a visco-elastic rheology for the compaction rate (see details in *Yarushina and Podladchikov* [2015]):

$$\nabla \cdot \vec{v_s} = -\beta_d \frac{d\overline{P}}{dt} + \left(\beta_d - \beta_s'\right)\frac{dP_f}{dt} - \frac{\overline{P} - P_f}{(1-\phi)\eta_\phi} \quad (9)$$

where β_d, β_s' and η_ϕ are respectively, the drained compressibility, the solid compressibility measured in an unjacketed test, and the pore viscosity.

3 General closed system of equations

Using Equations (7) and (9) to eliminate divergences of Darcian fluid flux and solid velocity from Equations (3) and (4) results in:

$$\frac{(1-\phi)\rho_n}{\rho_f}\frac{dR}{dt}+\frac{d_t\log\rho_f}{dt}+\left(\beta_d-\beta_s'\right)\frac{dP_f}{dt}=\nabla\cdot\frac{k_0\phi^3}{\mu_f}\left(\nabla P_f+\rho_f g\vec{e_z}\right)+\beta_d\frac{d\overline{P}}{dt}+\frac{\overline{P}-P_f}{(1-\phi)\eta_\phi} \quad (10)$$

$$\frac{1}{(1-\phi)}\frac{d\phi}{dt}=\frac{d\log(\rho_n)}{dt}-\beta_d\frac{d\overline{P}}{dt}+\left(\beta_d-\beta_s'\right)\frac{dP_f}{dt}-\frac{\overline{P}-P_f}{(1-\phi)\eta_\phi} \quad (11)$$

Equations (10) and (11) together with Equation (8) form a system of three equations for six unknowns (ϕ, P_f, $\overline{P}$, ρ_f, ρ_n, and R) under simplifying assumption $\frac{d}{dt}=\frac{\partial}{\partial t}$. Equilibrium thermodynamics is used to obtain three additional equations for ρ_f, ρ_n, and R as a function of P_f to close the system of equations. These three functions are tabulated as equations of state-type dependence on state variables pressure, temperature and composition of the solid in equilibrium with a free fluid phase. In contrast, the fluid volume fraction (porosity) can not be precomputed for a system open for fluid flow, since the amount of free fluid in excess of the saturation is not thermodynamically constrained. Hence, Equation (11) that combines mass balance and rheology becomes the evolution equation for porosity. The time derivatives of porosity were eliminated from Equations (3) and (10). The two remaining time derivatives of thermodynamically constrained ρ_f and R can be related to the fluid pressure time derivative leading to a parabolic equation for fluid pressure, P_f (see below). Finally, total pressure, $\overline{P}$, is obtained by depth integrating Equation (8).

The thermodynamically constrained ρ_f, ρ_n, and R were obtained from thermodynamic calculations performed with Gibbs free energy minimization software [e.g. Perple_X, *Connolly*, 2005] using the thermodynamic database of *Holland and Powell* [1998] (update 2002). Matlab™ scripts automated Perple_X calculations and extraction of relevant parameters (stable phase assemblage, densities, amount of chemically bound water in the solid).

3.1 Phases of fixed compositions and univariant reactions

Three different univariant reactions that typically occur in subduction zones are discussed here (Fig. 1): the dehydration of muscovite:

$$Muscovite + Quartz = Aluminosilicate + Sanidine + Water \quad (12)$$

$$KAl_3Si_3O_{10}(OH)_2 + SiO_2 = Al_2SiO_5 + KAlSi_3O_8 + H_2O, \quad (13)$$

the dehydration of serpentine:

$$Antigorite = Forsterite + Enstatite + H_2O \quad (14)$$

$$Mg_{48}Si_{34}O_{85}(OH)_{62} = 14Mg_2SiO_4 + 10Mg_2Si_2O_6 + 31H_2O, \quad (15)$$

and the decarbonation of calcite:

$$Calcite + Quartz = Wollastonite + CO_2 \quad (16)$$

$$CaCO_3 + SiO_2 = CaSiO_3 + CO_2 \quad (17)$$

These reactions are characterized by a sharp decrease of ρ_n and increase in R as volatile-bearing phases are produced (Fig. 1). The composition of the fluid does not evolve during these reactions. Therefore ρ_f is not sensitive to the devolatilization reactions and gradually varies in the whole P-T space (Supplementary Figure S1). Away from the reaction line, ρ_n increases with fluid pressure due to the solid compressibility (Fig. 1 A, C and E), while R decreases with fluid pressure as fluid is more compressible than solid (Fig. 1 B, D and F).

3.2 Solid solutions and multi-variant reactions

In natural rocks, solid phases are generally (non-ideal) mixtures rather than pure end-members. Taking into account solid solutions, univariant discontinuous (de-)volatilization reactions become multi-variant fields in P-T space in which devolatilization occurs continuously. As an example, three rock types typically found in the oceanic lithosphere and that may enter a subduction zone are discussed: sediments [*Plank and Langmuir*, 1998], mafic rocks [*Staudigel*

et al., 1996] and ultramafic rocks (harzburgite from *Schmidt and Poli* [1998]). For simplicity K_2O and TiO_2 are not considered for mafic and ultramafic rocks. The composition of these rocks used for thermodynamic modelling can be found in Table 2. For mafic and ultramafic rocks the fluid was modelled as pure water with the equation of state of *Holland and Powell* [1998], whereas H_2O-CO_2 mixtures were considered for the sediments. The solid solutions used for the three different rock composition are given in Table 3.

With multi-variant reactions, fluid density gradually increases with pressure and decreases with temperature for both pure water or an H_2O-CO_2 mixture (Fig. 2). For sedimentary rocks, an increase in density with temperature may occur when CO_2 proportion in the fluid increases due to rock decarbonation (e.g. at high pressure in Fig. 2 B). Complex variations in ρ_n are usual and reflect the complexity of the underlying phase diagrams (Fig. 3 A, C and E). For all the compositions, ρ_n displays the same general variation with the lowest values below 2900 $kg.m^{-3}$ at low P-T (<0.5 GPa and < 400 $^{\circ}C$) and the highest values above 3200 $kg.m^{-3}$ at high P-T (>3 GPa and > 700 $^{\circ}C$). This is due to an overall increase in solid density with pressure and a general increase in devolatilization with temperature (i.e. a decrease in rock bounded volatiles, X_s). A majority of the complexity of ρ_n disappears in the density ratio, R, which mainly decreases with fluid pressure (Fig. 3 B, D and F).

3.3 Densities and solid water content look-up tables

Solving Equations (10) and (11) can be done using look-up tables calculated with thermodynamic software such as Perple_X. The thermodynamic parameters tabulated as a function of pressure and temperature are shown in Figures 2 and 3. The advantage of this approach is that all complexity of the multi-variant reactions is captured and consistently coupled to the non-equilibrium processes. Although aqueous species are not taken into account in this contribution, the main factors controlling the fluid pressure and porosity evolution are the thermodynamic parameters shown in Figures 2 and 3, which are controlled by

the phase diagram topology. Current progress in calculating aqueous speciation for the P-T environments in metamorphic rocks suggests that phase diagrams are hardly affected by the dissolved components [*Galvez et al.*, 2015]. Therefore, it will not significantly affect the fluid pressure and porosity evolution.

3.4 Compressibilities

The pressure dependence of the thermodynamic parameters can be quantified by effective compressibilities:

$$\beta_f = \frac{d\log\rho_f}{dP_f} \quad (18)$$

$$\beta_R = \frac{dR}{dP_f} \quad (19)$$

$$\beta_s = \frac{d\log\rho_s}{dP_s} \approx \frac{\rho_n(1-\phi)}{\rho_f}\frac{dR}{d\bar{P}} \quad (20)$$

that can also be precomputed for usage as look-up tables.

Using the two above relationships (Equations (18) and (19)) in Equation (10), a parabolic equation for fluid pressure, P_f is obtained:

$$\beta_e\frac{dP_f}{dt} = \nabla\cdot\left(\frac{k_0\phi^3}{\mu_f}\left(\nabla P_f + \rho_f g\vec{e_z}\right)\right) + (\beta_d - \beta_s)\frac{d\bar{P}}{dt} + \frac{\bar{P}-P_f}{(1-\phi)\eta_\phi} \quad (21)$$

with the effective compressibility expressed as:

$$\beta_e = \beta_d - \beta_s' + \beta_f + \beta_R\frac{(1-\phi)\rho_n}{\rho_f} \quad (22)$$

The first term in the right-hand side of Equation (21) is the Darcy's flux, the second and third term are related to, respectively, the elastic and viscous response of the rock to deformation. In the effective compressibility β_e, the impact of reaction on changes in fluid pressure are accounted for by β_f and β_R.

The other compressibilities in β_e are related to elastic deformation. In section 4.3 this effective compressibility is shown to be positive which allows Equation (21) to be solved numerically.

4 Special simplified cases

The general system is very complex and non-transparent. In order to see familiar effects the simplified limits are considered. First, introducing a shorthand notation for the total density, $\overline{\rho}$:

$$\overline{\rho} = \phi\rho_f + (1-\phi)\rho_s \qquad (23)$$

results in an equivalent form of the total mass conservation equation (3) useful for the forthcoming simplifications:

$$\frac{d\overline{\rho}}{dt} + \overline{\rho}\nabla\cdot\vec{v_s} + \nabla\cdot\left(\rho_f\phi\left(\vec{v_f} - \vec{v_s}\right)\right) = 0 \qquad (24)$$

4.1 No reaction

Without reaction there is no fluid mass transfer between the solid and the fluid. In this case the time derivative of X_s is equal to zero and Equations (10) and (11) can be simplified by eliminating X_s. The equations become identical to the ones in *Yarushina and Podladchikov* [2015]. In the pure elastic case (infinite viscosity) the Biot poro-elastic limit is recovered. In the pure viscous and more complex visco-elastic cases the non-reactive equations are equivalent to the porosity wave equations with well established properties [*Richter and McKenzie*, 1984; *Scott and Stevenson*, 1986; *Connolly and Podladchikov*, 1998, 2007, 2013, 2015].

4.2 Non-deforming solid

In the case of highly permeable rocks (near-surface conditions), changes of fluid pressure due to reactions will induce fluid flow rather than rock deformation leading to the assumption of negligible deformation of the solid ($\nabla\cdot\vec{v_s} = 0$). As

shown in Appendix (B), under this assumption, the porosity and the total density can be constrained by thermodynamic properties only:

$$\phi = 1 - \frac{\rho_n^0 \left(1 - \phi_0\right)}{\rho_n} \qquad (25)$$

and

$$\bar{\rho} = \rho_f + R\rho_n^0 \left(1 - \phi_0\right) \quad (26)$$

with ρ_n^0 and ϕ_0 two time integration 'constants' that can be functions of the spatial coordinates. These latter equations can be used to simplify Equation (24) to obtain the following fluid pressure time derivative:

$$\rho_f \beta_e \frac{dP_f}{dt} = \nabla \cdot \left(\frac{\rho_f k}{\mu_f} \left(\nabla P_f + \rho_f g \overrightarrow{e_z} \right) \right) \quad (27)$$

with

$$\beta_e = \beta_f + \beta_R \frac{\left(1 - \phi_0\right) \rho_{n0}}{\rho_f} \qquad (28)$$

Now, the effective compressibility contains only terms related to the effect of reaction on fluid pressure (compare with Equation (22)). The associated changes in fluid pressure induce fluid flow (right-hand side of Equation (27)).

4.3 No fluid flow

A closed system approximation (no Darcy's flux; $\nabla \cdot \left(\phi \left(\overrightarrow{v_f} - \overrightarrow{v_s} \right) \right) = 0$) is valuable for some systems in which fluid is released extremely fast before fluid flow can occur (*e.g.* incipient reaction with a high amount of released fluid).

As shown in Appendix (C), the porosity and the total density can be expressed as a function of thermodynamic parameters only:

$$\phi = 1 - \frac{\rho_f}{C_o \rho_n + \rho_f - \rho_s} \qquad (29)$$

and

$$\overline{\rho} = \frac{\rho_f C_o}{\left(C_o - R\right)} \quad (30)$$

with C_o a constant such as:

$$C_o = \frac{\overline{\rho}_0}{\rho_{n0}\left(1 - \phi_0\right)} \qquad (31)$$

Under the assumption of constant fluid density and using Equation (30), the pressure derivative of the system volume (the inverse of the total density) is:

$$\frac{d\left(\frac{1}{\overline{\rho}}\right)}{dP_f} = \frac{dV}{dP_f} = -\frac{\rho_n\left(1-\phi\right)}{\overline{\rho}\rho_f}\frac{dR}{dP_f} \qquad (32)$$

This allows to express the compressibility of R as:

$$\beta_R = -\frac{\overline{\rho}\rho_f}{\rho_n\left(1-\phi\right)}\frac{dV}{dP_f} \quad (33)$$

During reaction, the change in the system volume (dV) with increasing pressure is always negative. For positive Clapeyron slopes hydration occurs with increasing pressure. The hydrous phases occupy a smaller volume than anhydrous phases and fluid and therefore system volume change is negative. For negative Clapeyron slopes dehydration occurs with increasing the pressure, which produces anhydrous phases and fluid that occupy a smaller volume than the hydrous phases (Fig. 4), also resulting in a negative change in system volume (dV). Therefore, β_R is always positive and the parabolic equation for fluid pressure can be solved numerically (Equation (21)).

Substituting $\bar{\rho}$ expression from Equation (30) to derive the reaction effect on volume in a closed system, $\Delta_r V$:

$$\Delta_r V = \Delta_r \frac{1}{\bar{\rho}} = \Delta_r \frac{1}{\rho_f} - \frac{1}{C_0}\left(\Delta_r \frac{1}{\rho_n} + \Delta_r \frac{1}{\left(1 - X_s\right)\rho_f} \right) \quad (34)$$

that can be simplified in the case of constant fluid density:

$$\Delta_r V = \frac{\left(1-\phi_0\right)}{\bar{\rho}_0}\left(-\frac{\Delta\rho_n}{\rho_n} + \frac{\rho_{n_0}}{\rho_f}\frac{X_{s_0} - X_s}{\left(1 - X_{s_0}\right)\left(1 - X_s\right)} \right) \quad (35)$$

which is verified by comparison with the volumetric effect of reaction calculated with Perple_X under the same closed system constraint (Fig. 5 and Supplementary Figure S2). The volume change during a reaction expressed in Equation (35) also appears in the expression of the Clapeyron slope:

$$\frac{dT}{dP_f} = \frac{\Delta_r V}{\Delta_r S}. \quad (36)$$

Figure 5 shows that the Clapeyron slope calculated with the volume change of Equation (35) is equivalent to the one calculated with Perple_X. During devolatilization reactions at constant pressure and increasing temperature, the produced fluid has a higher entropy than the rock ($\Delta_r S > 0$). Therefore, as the Clapeyron slope of the considered reactions are positive at pressure below ~ 2.5 GPa (Fig. 5), the total volume increases. The reversal of the Clapeyron slope of antigorite dehydration above ~ 2.5 GPa occurs during a change in sign of the volume change of the reaction (Fig. 5). This is associated with a higher compressiblity of water compared to the solid in this pressure range.

The pressure anomaly due to a reaction is generally estimated in a closed system (no Darcy's flux) for univariant reactions [e.g. *Kelemen and Hirth*, 2012; *Tian and Ague*, 2014]. Introducing the relationship between the

volume of the system and its density ($V = \frac{1}{\bar{\rho}}$) and Equation (9) in the case of purely elastic deformation with the assumption of lithostatic pressure ($\nabla \cdot \vec{v_s} = \left(\beta_d - \beta_s'\right) \frac{dP_f}{dt}$) into Equation (24) gives an expression of the pressure change associated with the volume change during reaction:

$$\Delta_r P = \frac{1}{\beta_d - \beta_s'} \frac{\Delta_r V}{V} \quad (37)$$

This pressure change is a maximum since it is estimated in a closed system with a univariant reaction in which (de)volatilization occurs abruptly when crossing the reaction line.

4.4 Constant densities of solid phases

In Equations (1) and (2), the solid is divided in species (*i.e.* volatile species bound to the solid and non-volatile species such as Si or Mg). The system can also be decomposed in volatile-bearing and volatile-free phases with different densities, ρ_h and ρ_a, respectively. Volatile-free phases and fluid are formed during the reaction of volatile-bearing phases.

This choice of decomposition of the system in phases has several advantages in recognizing reasonable assumptions for solving Equations (10) and (11):

1. Hydrous phases contain an amount of water, X_h, which varies less than the amount of water in the rock, X_s (Fig. 6 and Supplementary Figure S3). For ultramafic rocks, the amount of water in antigorite varies within 0.13 *wt.*% whereas the amount of water in the solid varies by more than 11 *wt.*%. For mafic rocks, the amount of water in chlorite varies within 0.75 *wt.* % while the amount of water in the solid varies by approximately 4 *wt.*%. For sedimentary rocks, the amount of carbon dioxide in calcite varies within 0.07 *wt.*% whereas the amount of water and carbon dioxide

in the solid varies by approximately 7 *wt*.%. Based on these quantitative data, we adopted in the following the assumption of constant X_h.

2. The density of the volatile-bearing phases is less variable than the solid density (Fig. 6 and Supplementary Figure S4). For example, the density of volatile-bearing phases calculated for the sedimentary rock varies by 9% whereas the density of the solid varies by 15%. The densities of the volatile-bearing phases, ρ_h, and of the volatile-free phases, ρ_a were assumed to be constant in the following. Although these approximations are rough in the case of only one hydrous phase (Fig. 6), it reproduces solid density relatively well when several hydrous phases are considered. The case for a single hydrous phase is first treated here because it provides a clear link between volume change of reaction and the associated porosity and fluid pressure changes. A more complex derivation for multiple hydrous phases is presented in Appendix D.

The amount of fluid in the rock can either be expressed directly using the amount of water in the rock, X_s, or with the amount of hydrous phases in the rock, S_h, containing an amount of water of X_h:

$$\rho_s X_s = \rho_h X_h S_h \qquad (38)$$

Moreover, the solid is composed of hydrous and anhydrous phases, and its density can thus be expressed as:

$$\rho_s = \rho_a \left(1 - S_h\right) + \rho_h S_h \quad (39)$$

Equations (38) and (39) can be used to remove ρ_s and X_s from the expression of ρ_n:

$$\rho_n = \rho_h S_h \left(1 - X_h\right) + \rho_a \left(1 - S_h\right). \qquad (40)$$

and R:

$$R = 1 + \frac{\rho_h X_h S_h - \rho_f}{\rho_a \left(1 - S_h\right) + \rho_h S_h \left(1 - X_h\right)} \qquad (41)$$

which becomes functions of S_h.

To solve Equations (10) for fluid pressure at constant fluid density, the time derivative of R has to be expressed as a function of the time derivative of fluid pressure. This requires to express the time derivative of S_h (Equation (41)).

We used an exponential function to fit S_h to fluid pressure (Fig. 7):

$$S_h \approx S_h^{max} - \left(S_h^{max} - S_h^{min}\right)\left(e^{-\beta_h\left(P_f - P_r\right)}\right) \qquad (42)$$

with a constant, β_h, which is positive when S_h increases with fluid pressure (positive Clapeyron slope) and negative when it decreases with fluid pressure (negative Clapeyron slope). The use of such a fit is justified by the definition of the chemical potential which directly relates the amount of volatile species or hydrous phases to a fluid pressure exponential [*Tajčmanová et al.*, 2014]. During hydration of ultramafic rocks, this function predicts an increase of S_h with pressure which diverges by less than 5 % from the calculated data (Fig. 7). For dehydration of ultramafic rocks, the predicted S_h diverges by less than 10 % from the data (Fig. 7).

Using Equations (41) and (42), the time derivative of R is:

$$\frac{dR}{dt} = -\frac{1}{\rho_n}\frac{d\rho_f}{dt} + \frac{\rho_a \rho_f}{\rho_n^2}\rho_h \Delta_r V \frac{dS_h}{dt} \qquad (43)$$

In Equation (43), the change in volume due to reaction, $\Delta_r V$, corresponds to:

$$\Delta_r V = \frac{1 - X_h}{\rho_a} + \frac{X_h}{\rho_f} - \frac{1}{\rho_h} \qquad (44)$$

Equation (44) is the change in volume for a dehydration reaction in an initially non-porous rock ($\phi_0 = 0$) obtained from a chemical reaction by taking the difference in volume of products and reactants. It is obtained with Equation (35) for the change in volume at constant fluid density by considering the following assumptions. Before dehydration, all volatiles are stored in hydrous phases. The initial proportion of chemically bound fluid in the solid is therefore equal to the proportion of fluid in the hydrous phase ($X_{s_0} = X_h$) and the initial amount of non-volatile species is equal to the initial amount of non-volatile species in the hydrous phases ($\rho_{n_0} = \rho_h (1 - X_h)$). When dehydration is complete, there are no hydrous phases left and all volatile species are in the fluid (X_s = 0 and $\rho_n = \rho_a$). The change in volume expressed in Equation (44) is the same as the one used to calculated Clapeyron slopes and is thus positive for positive Clapeyron slopes and negative for negative Clapeyron slopes. Equation (43) indicates that, as $\frac{dS_h}{dP_f}$ has the same sign as $\Delta_r V$ (Fig. 4), R increases with pressure where reaction occurs and decreases with pressure everywhere else due to fluid compressibility. This is in agreement with calculations of R variations for univariant reactions (Fig. 1).

Introducing Equation (43) in Equation (10), the parabolic equation for fluid pressure given in Equation (21) is obtained but with another expression for effective compressibility:

$$\beta_e = \beta_d - \beta_s' + \phi\beta_f + \frac{\rho_a (1-\phi)}{\rho_n} \left(S_h^{max} - S_h \right) \rho_h \Delta_r V \beta_h \quad (45)$$

The $\Delta_r V \beta_h$ product is always positive since $\Delta_r V$ and β_h are both negative for reactions with negative Clapeyron slopes and positive for reactions with positive Clapeyron slopes (Fig. 4). Therefore, β_e is positive. This will avoid numerical instabilities when solving Equation (21) [*Hirt*, 1968].

5 Numerical modelling of infiltration in reacting porous media

The behaviour of the above equations was investigated using an explicit finite difference approach. Thermodynamic data for the three initial compositions used here (ultramafic, mafic and sedimentary rocks) were used as input parameters for the numerical models (Fig. 8). Pressure and temperature range was set around target reactions with different properties: (1) antigorite dehydration with a negative Clapeyron slope for the ultramafic rocks, (2) chlorite dehydration with a positive Clapeyron slope for the mafic rocks, (3) decarbonation with a positive Clapeyron slope and a fluid as a H_2O-CO_2 mixture for the sedimentary rocks (Fig. 8). The variations of the thermodynamic parameters were modelled with compressibilities which were either fitted to the data (R parameter for ultramafic rocks; Fig. 8) or estimated with look-up tables (R parameter for mafic and sedimentary rocks; Fig. 8 and ρ_n for all the compositions). Simulations without deformation were done to see the first order impact of reaction on porosity and fluid pressure. Finally, the coupling between reaction and deformation were investigated by introducing elastic deformation.

An initial fluid pressure anomaly is setup in the center of the model domain at constant temperature. The generation of these anomalies was not the focus of the modelling and may be associated with mineralogical reactions in the vicinity of the studied zone or with deformation (e.g. earthquake, tectonic deformation or thermal contraction). Negative and positive pressure changes were investigated. The simulations predict evolution of the fluid pressure and associated porosity changes.

5.1 Modelling without deformation

Fluid pressure, porosity and mineralogical changes computed in one dimension are presented in Figure 9 (two and three dimensional models were also produced (see Supplementary Figure S5) but one dimensional models are sufficient to discuss the solution to the equations describing the coupled reactive porous flow). For the ultramafic rock, the model gives equivalent results in case of using a fit or look-up tables to estimate variations in compressibility (red and black

lines, respectively, in Fig. 9A). A model in which reaction is not considered produces a very limited evolution in pressure with time (green lines in Fig. 9). As the solid density can not change in non-reactive models, porosity can not be generated and permeability remains too low to allow sufficient fluid flow. It clearly shows how reactions play a critical role in generating fluid pathways during metamorphism.

The fluid pressure variation is either smooth (Fig. 9 E and I) or abrupt (Fig. 9A) depending on the investigated reaction. The shape of the pressure profile depends on the permeability distribution. In case permeability is higher at the border of the profile, smooth profiles will be obtained whereas if the permeability is higher in the center of the profile, abrupt profiles will be obtained. Variations in permeabilities are directly related to variations in porosity through Equation (7) which are themselves related to variations in ρ_n through a simplified version of Equation (4) in case of no deformation (Equation (25)).

Variations in ρ_n, and thus in porosity, are controlled by variations in the solid density, ρ_s and fluid amount in the solid, X_s (Fig. 8 and Equation (5)). These variations depend on the Clapeyron slope of the reaction. For positive Clapeyron slopes, volatile-bearing phases are produced when fluid pressure increases. X_s therefore increases and ρ_s decreases resulting in a decrease of ρ_n. Following Equation (25) relating ρ_n to porosity in the non-deforming case, the porosity therefore decreases when the fluid pressure increases for positive Clapeyron slopes. As a result, the porosity and associated permeability are low at high fluid pressure (Fig. 9) and decreasing the fluid pressure will allow faster fluid transport. This results in smooth profiles of pressure relaxation from an initial positive anomaly in the center (Fig. 10 E and F). An initial negative pressure anomaly causes abrupt pressure variations with a sharp reaction front (Fig. 10 E and F). For negative Clapeyron slopes, volatile-free phases are produced when fluid pressure increases resulting in a decrease of X_s and an increase of ρ_s. ρ_n, porosity and permeability therefore increase with fluid pressure (Fig. 8 and

Equation (25)). As a result, an opposite trend is observed compared to positive Clapeyron slopes with a positive pressure anomaly relaxed through the propagation of a sharp reaction front (Fig. 10 A and B) and a negative pressure anomaly relaxed through smooth pressure variations in space (Fig. 10 C and D).

5.2 Numerical model with deformation

Deformation was investigated for purely elastic behaviour of the solid (neglecting the viscous term in Equation (9)) during chlorite and antigorite dehydrations (Fig. 11). Considering the impact of reaction and/or deformation resulted in different profiles for fluid pressure relaxation compared to the common approximation of fluid flow in a rock with a fixed background porosity (orange lines in Fig. 11) suggesting that the equations introduced here are fundamental to understand fluid flow in reactive rocks. The combined effect of reaction and deformation on fluid flow depends on the Clapeyron slope of the reaction.

As shown in the previous section, reactions with a negative Clapeyron slope are associated with a porosity increase with fluid pressure. Moreover, as fluid pressure increases pore space expands (Equation (11)) resulting in an increase of porosity with fluid pressure. Therefore, reaction and deformation induce porosity variations in the same direction for negative Clapeyron slopes. As a result, the shape of the pressure and porosity profiles do not depend on the value of $\beta_d - \beta_s'$ (green and blue lines in Fig. 11 A and B) and the porosity front propagates faster when reaction and deformation are both considered (green and blue lines compared to cyan and red lines, respectively, in Fig. 11 B).

For positive Clapeyron slopes as fluid pressure increases porosity increases due to deformation but also decreases due to reaction (see previous section). As a result, the porosity front propagates slower when reaction and deformation are both considered (green and blue lines compared to cyan and red lines, respectively, in Fig. 11 D). Moreover, the shape of pressure and porosity profiles depend on the value of $\beta_d - \beta_s'$. When the system evolution is controlled by

deformation (high $\beta_d - \beta_s'$ values), the profiles are similar to the profiles obtained with negative Clapeyron slopes (green lines in Fig. 11 C and D). For values of $\beta_d - \beta_s'$ where the impacts of reaction and deformation are of the same order of magnitude, porosity varies on a smaller range than for purely reactive or elastic models. Intermediate profiles between these two end-members are obtained with parts of the porosity profile displaying an increase of porosity with pressure and other parts displaying a decrease of porosity with pressure (blue line in Fig. 11 D). As $\beta_d - \beta_s'$ is fixed in the model, the location of these various parts depends on the impact of reaction on porosity and, following Equation (11), on the variations of ρ_n with fluid pressure. For low $\frac{d\rho_n}{dP_f}$, the evolution of porosity will be dominated by deformation whereas, for high $\frac{d\rho_n}{dP_f}$, it will be dominated by reaction (blue line in Fig. 11 D and E). This results in complex patterns for porosity and fluid pressure evolution different from the one obtained when considering fluid flow only (Fig. 11 C and D).

6 Discussion and Conclusion

Source terms taking into account the transfer of volatile species between solid and fluid have been introduced in mass conservation equations by several authors [*Connolly*, 1997; *Wilson et al.*, 2014]. Expressions of these source terms were formulated both in the non-equilibrium and in the equilibrium cases. *Connolly* [1997], *Spiegelman et al.* [2001], *Hesse et al.* [2011] and *Liang et al.* [2011] used a source term which was a linear function of the distance from the equilibrium and of the reactive surface area. *Wilson et al.* [2014] introduced a source term which corresponds to the change in water content in the rock when modifications of the P-T conditions occur. The water content in the rock was calculated as a function of pressure and temperature based on equilibrium thermodynamic calculations, similar to the approach presented here. The main difference between most of these previous models and our approach is that we do not assume constant density of the solid. Another difference with some of the

previous work lies in the general formulation of the approach with look-up tables, which is not restricted to modelling one or several manually selected reactions.

An increase in solid density by approximately 30% is calculated during the release of volatile species in subduction zones [*Hacker*, 2003]. An explanation for this change in solid density is that volatile species such as water or carbon dioxide occupy a larger volume than other species (oxides) when they are bound in minerals like clays or carbonates. To deal with these changes, we proposed to introduce three thermodynamic parameters, R, ρ_n and ρ_f. These parameters can be precomputed in look-up tables for both univariant and multi-variant reactions to solve the parabolic equation of fluid pressure variation obtained when replacing thermodynamic parameters variations with compressibilities (Equation (21)). This equation is equivalent to the equation derived for non-reactive fluid flow [*Yarushina and Podladchikov*, 2015] but with an additional reactive term accounting for porosity and fluid pressure changes due to reaction. In this Equation, the effective compressibility in front of the fluid pressure time derivative is positive since β_R has a positive sign as shown with the closed system assumption. This parabolic equation is still valid with approximations but with other expressions for the effective compressibility. These approximations both give a better physical understanding of the equations and a confirmation on the numerical stability of Equation (21):

1. Without deformation, Equation (10) can be simplified by introducing the total density and the porosity becomes a simple function of thermodynamic parameters only.
2. In a closed system, an equation relating the change in pressure to the change in volume is obtained (Equation (37)). This equation recalls an expression for compressibility [*Turcotte and Schubert*, 2014] in which pressure and volume changes depend on the reaction and are related through pore compressibility ($\beta_d - \beta_s'$). Volume change during reaction can be as high as several tens of percent and pore compressibility has a

typical value of 10^{-9} Pa^{-1} [*Connolly and Podladchikov*, 1998]. Therefore, the maximum pressure rise in a closed system is on the order of several tenths of GPa. This value is of the same order of magnitude as the one given by *Kelemen and Hirth* [2012] for olivine serpentinization.

3. With the decomposition of the solid in phases of constant density, the reactive term in the effective compressibility can be expressed as a function of the change in volume during reaction, a variable which is commonly used when discussing changes in fluid pressure and in porosity during reaction. Moreover, this reactive term is found to be always positive preventing the generation of instabilities when numerically solving Equation (21).

One, two and three dimensions numerical models were constructed either by approximating variations in R with compressibility or by using look-up tables. Results did not depend on the dimension and on the method used to determine the variations in R. The shape of the pressure profile depends on the initial pressure gradient between the border and the center of the model and on the relationship between the permeability and the fluid pressure. This latter relationship depends on the Clapeyron slope with high permeability at low fluid pressure for positive Clapeyron slope and at high fluid pressure for negative Clapeyron slope. In other models of porosity waves, a background porosity is fixed and the reorganization of this porosity as a result of deformation and fluid flow is investigated [*Connolly and Podladchikov*, 2013]. With the new model of reacting porosity waves presented here, porosity can be generated in a non porous rock as a result of reaction allowing porous flow to occur in an initially fluid-free rock. When elastic deformation is also considered, the porosity front propagates faster for reactions with negative Clapeyron slope and slower for reactions with positive Clapeyron slope.

The equations presented here fully respect conservation of mass and improve modelling the interplay between reaction, deformation and fluid flow from a

thermodynamic point of view. However, still development is required to further improve the modelling of natural processes. First, non-volatile species can be transported in the rock as aqueous species by advection or diffusion in the fluid. This is particularly important for long-term metasomatism during which over time significant amounts of dissolved species may be transported along chemical potential gradients between rock of different compositions. Aqueous species transport will modify the bulk composition of the solid and the associated thermodynamic equilibrium. Considering such transport of aqueous species requires to be able to model the composition of an aqueous solution at the equilibrium with a solid. This is currently possible at pressures below 0.5 GPa for example with the database of *Johnson et al.* [1992]. However, at high pressure, thermodynamic models like Perple_X do not allow such calculations due to the limitations in pressure of the used equations of state such as the revised Helgeson-Kirkham-Flowers (HKF) equations of state [*Helgeson et al.*, 1981]. Recent thermodynamic developments allow to consider more complex fluids at high pressure [*Mantegazzi et al.*, 2013; *Sverjensky et al.*, 2014] and their incorporation in thermodynamic softwares considering aqueous species [e.g. *Kulik et al.*, 2013] allows modelling systems undergoing compositional changes due to metasomatic processes.

Mineralogical reactions are time-dependent processes having kinetics. The achievement of thermodynamic equilibrium and, thus, the changes in fluid pressure and in porosity associated with reaction will be delayed by these kinetics. Although some authors have proposed that the rate of metamorphic reaction is rather controlled by the transport of fluid than by the kinetics of reaction [*Carlson*, 2011], quantitative estimates of the interplay between fluid flow and kinetics are still lacking. Introducing a kinetic delay in the achievement of thermodynamic equilibrium in the formalism described here is needed to do these estimates.

Other deformation processes important for fluid transport will also have to be simulated. For example, viscous compaction allows to generate solitary porosity waves with a higher speed [*Connolly and Podladchikov*, 1998] and fracturing and shear deformation generate fluid pathways increasing permeability and the kinetics of reaction [*Jamtveit et al.*, 2009; *Plümper et al.*, 2012; *Austrheim and Griffin*, 1985].

Appendix A: Mass conservation equations with thermodynamic parameters

The aim of this appendix is to show the rearrangement of the equations for conservation of total and non-volatile mass into the form presented in respectively Equations (3) and (4).

For completeness the starting point of the derivation is repeated here, with the conservation of total mass:

$$\frac{\partial\left(\rho_f\phi+\rho_s\left(1-\phi\right)\right)}{\partial t}+\nabla\cdot\left(\rho_f\phi\overrightarrow{v_f}+\rho_s\left(1-\phi\right)\overrightarrow{v_s}\right)=0 \qquad \text{(A1)}$$

and the conservation of non-volatile mass:

$$\frac{\partial\left(\rho_s\left(1-X_s\right)\left(1-\phi\right)\right)}{\partial t}+\nabla\cdot\left(\rho_s\left(1-X_s\right)\left(1-\phi\right)\overrightarrow{v_s}\right)=0. \qquad \text{(A2)}$$

Equation (A1) is designated to become the pressure evolution equation and porosity evolution is governed by Equation (A2). To achieve this porosity time derivatives are solved in one equation and eliminated in the other. Additionally, it is convenient to separate the unknowns related only to equilibrium thermodynamics from quantities governed by non-equilibrium processes. This leads to terms related to fluid flow (Darcy flux) and solid deformation (divergence of velocity) separated from terms governing density changes in fluid and solid.

In the following sequence of steps to isolate the time derivative of porosity $\frac{d\phi}{dt}$ material derivatives ($\frac{d}{dt}=\frac{\partial}{\partial t}+\vec{v_s}\cdot\nabla$) are used. The material derivative describes the time rate of change of some physical quantity (like heat or momentum) for a material element subjected to a space-and-time-dependent macroscopic velocity field. Here the porosity is followed in a certain solid parcel in time as it is being moved along with the solid. Therefore solid velocity is used in the material derivatives unless otherwise stated.

Adding and subtracting $\nabla\cdot\rho_f\phi\vec{v_s}$ equation (A1) is re-written:

$$\frac{\partial\overline{\rho}}{\partial t}+\nabla\cdot\left(\rho_f\phi\vec{v_f}-\rho_f\phi\vec{v_s}+\rho_f\phi\vec{v_s}+\rho_s\left(1-\phi\right)\vec{v_s}\right)=0 \qquad \text{(A3)}$$

This allows recognizing material derivative of total density, and terms related to fluid flow $\phi\left(\vec{v_f}-\vec{v_s}\right)$ and deformation $\nabla\cdot\vec{v_s}$:

$$\frac{\partial\overline{\rho}}{\partial t}+\nabla\cdot\left(\rho_f\phi\left(\vec{v_f}-\vec{v_s}\right)\right)+\vec{v_s}\cdot\nabla\overline{\rho}+\overline{\rho}\nabla\cdot\vec{v_s}=0 \qquad \text{(A4)}$$

By replacing partial time derivatives by material derivatives, Equation (A4) becomes:

$$\frac{d\overline{\rho}}{dt}+\overline{\rho}\nabla\cdot\vec{v_s}+\nabla\cdot\left(\rho_f\phi\left(\vec{v_f}-\vec{v_s}\right)\right)=0 \qquad \text{(A5)}$$

The total mass as defined in the time derivative in Equation (A1) can be re-arranged to isolate porosity, as the main target is to eliminate its material derivative. It is therefore rewritten as:

$$\overline{\rho}=\rho_f+\left(1-\phi\right)\left(\rho_s-\rho_f\right) \qquad \text{(A6)}$$

Taking the derivative of $\overline{\rho}$ (equivalent to expanding the material derivative of $\overline{\rho}$ into terms) gives:

$$\frac{d\bar{\rho}}{dt}=\frac{d\rho_f}{dt}+(1-\phi)\frac{d\left(\rho_s-\rho_f\right)}{dt}-\left(\rho_s-\rho_f\right)\frac{d\phi}{dt}. \qquad \text{(A7)}$$

Substituting into Equation (A5) leads to the desired result of isolating $\frac{d\phi}{dt}$ in Equation (A1):

$$\frac{d\rho_f}{dt}+(1-\phi)\frac{d\left(\rho_s-\rho_f\right)}{dt}-\left(\rho_s-\rho_f\right)\frac{d\phi}{dt}+\nabla\cdot\left(\rho_f\phi\left(\overrightarrow{v_f}-\overrightarrow{v_s}\right)\right)+\rho_t\nabla\cdot\overrightarrow{v_s}=0 \qquad \text{(A8)}$$

Equation (A2) is now solved for $\frac{d\phi}{dt}$ to eliminate it from Equation (A8).

Expanding the divergence term in Equation (A2) to recognize the material derivative of non-volatile mass:

$$\frac{\partial\left(\rho_s\left(1-X_s\right)(1-\phi)\right)}{\partial t}+\rho_s\left(1-X_s\right)(1-\phi)\nabla\cdot\overrightarrow{v_s}+\overrightarrow{v_s}\cdot\nabla\left(\rho_s\left(1-X_s\right)(1-\phi)\right)=0 \qquad \text{(A9)}$$

Substituting the material derivative:

$$\frac{d\left(\rho_s\left(1-X_s\right)(1-\phi)\right)}{dt}+\rho_s\left(1-X_s\right)(1-\phi)\nabla\cdot\overrightarrow{v_s}=0 \qquad \text{(A10)}$$

Isolating the divergence of solid velocity gives:

$$\frac{1}{\rho_s\left(1-X_s\right)(1-\phi)}\frac{d\left(\rho_s\left(1-X_s\right)(1-\phi)\right)}{dt}+\nabla\cdot\overrightarrow{v_s}=0 \qquad \text{(A11)}$$

The mass of the non-volatile components (i.e. every component that does not enter the fluid during reaction) is defined as:

$$\rho_n=\rho_s\left(1-X_s\right) \qquad \text{(A12)}$$

Substituting Equation (A12) into Equation (A11) and simplifying gives the final equation for the conservation of non-volatile mass given in the main text (see Equation (4)):

$$\frac{d\log\left(\rho_n(1-\phi)\right)}{dt}+\nabla\cdot\vec{v_s}=0 \quad \text{(A13)}$$

To solve for $\frac{d\phi}{dt}$ it is convenient to substitute Equation (A12) into Equation (A10):

$$\frac{d\left(\rho_n(1-\phi)\right)}{dt}+\rho_n(1-\phi)\nabla\cdot\vec{v_s}=0 \quad \text{(A14)}$$

Expanding the material derivative in Equation (A14) to isolate $\frac{d\phi}{dt}$:

$$(1-\phi)\frac{d\rho_n}{dt}-\rho_n\frac{d\phi}{dt}+\rho_n(1-\phi)\nabla\cdot\vec{v_s}=0 \quad \text{(A15)}$$

Solving for $\frac{d\phi}{dt}$ gives after some simplification:

$$\frac{d\phi}{dt}=\frac{(1-\phi)}{\rho_n}\frac{d\rho_n}{dt}+(1-\phi)\nabla\cdot\vec{v_s} \quad \text{(A16)}$$

Equation (A16) can be introduced into Equation (A8):

$$\frac{d\rho_f}{dt}+(1-\phi)\frac{d\left(\rho_s-\rho_f\right)}{dt}-\left(\rho_s-\rho_f\right)\left(\frac{(1-\phi)}{\rho_n}\frac{d\rho_n}{dt}+(1-\phi)\nabla\cdot\vec{v_s}\right)+\nabla\cdot\left(\rho_f\phi\left(\vec{v_f}-\vec{v_s}\right)\right)+\rho_t\nabla\cdot\vec{v_s}=0 \quad \text{(A17)}$$

Collecting solid fraction $(1-\phi)$ will separate parameters dealing only with equilibrium thermodynamics from the other parameters.

$$\frac{d\rho_f}{dt}+(1-\phi)\left(\frac{d\left(\rho_s-\rho_f\right)}{dt}-\frac{\left(\rho_s-\rho_f\right)}{\rho_n}\frac{d\rho_n}{dt}-\left(\rho_s-\rho_f\right)\nabla\cdot\vec{v_s}\right)+\nabla\cdot\left(\rho_f\phi\left(\vec{v_f}-\vec{v_s}\right)\right)+\rho_t\nabla\cdot\vec{v_s}=0 \quad \text{(A18)}$$

Choosing a parameter R as:

$$R=\frac{\rho_s-\rho_f}{\rho_n}. \quad \text{(A19)}$$

With its derivative:

$$\frac{dR}{dt} = -\left(\rho_s - \rho_f\right)\frac{1}{\rho_n{}^2}\frac{d\rho_n}{dt} + \frac{1}{\rho_n}\frac{d\left(\rho_s - \rho_f\right)}{dt} \quad \text{(A20)}$$

Equilibrium thermodynamic parameters in Equation (A18) which vary greatly during reactions can now be conveniently grouped into one time derivative $\frac{dR}{dt}$:

$$\frac{d\rho_f}{dt} + \left(1-\phi\right)\rho_n\frac{dR}{dt} - \left(1-\phi\right)\left(\rho_s - \rho_f\right)\nabla\cdot\overrightarrow{v_s} + \nabla\cdot\left(\rho_f\phi\left(\overrightarrow{v_f} - \overrightarrow{v_s}\right)\right) + \rho_t\nabla\cdot\overrightarrow{v_s} = 0 \quad \text{(A21)}$$

Substituting $\overline{\rho}$ from Equation (A6) into Equation (A21) above, allows simplification:

$$\frac{d\rho_f}{dt} + \left(1-\phi\right)\rho_n\frac{dR}{dt} + \nabla\cdot\left(\rho_f\phi\left(\overrightarrow{v_f} - \overrightarrow{v_s}\right)\right) + \rho_f\nabla\cdot\overrightarrow{v_s} = 0 \quad \text{(A22)}$$

The equation above contains now the desired result, the first term just dealing with density of the fluid, the second term dealing with equilibrium thermodynamic parameters only, and the last two terms related to fluid flow and solid deformation respectively.

Note that by introducing a material derivative for the total system ($\frac{d_t}{dt} = \frac{\partial}{\partial t} + \left(\phi\overrightarrow{v_f} + \left(1-\phi\right)\overrightarrow{v_s}\right)\cdot\nabla$), Equation (3) given in the main text is obtained:

$$\frac{\left(1-\phi\right)\rho_n}{\rho_f}\frac{dR}{dt} + \frac{1}{\rho_f}\frac{d_t\rho_f}{dt} + \nabla\cdot\overrightarrow{v_s} + \nabla\cdot\left(\phi\left(\overrightarrow{v_f} - \overrightarrow{v_s}\right)\right) = 0. \quad \text{(A23)}$$

Appendix B: Simplifications when assuming no deformation

Considering negligible deformation of solid is equivalent to:

$$\nabla\cdot\overrightarrow{v_s} = 0 \qquad \text{(B1)}$$

that requires $\beta_d = \beta_s' = \frac{1}{\eta_\phi} = 0$. This simplifies Equation (4) to:

$$\frac{d\left(\rho_n\left(1-\phi\right)\right)}{dt} = 0 \qquad \text{(B2)}$$

Time integrating:

$$\rho_n\left(1-\phi\right) = C_0 = \rho_n^0\left(1-\phi_0\right) \qquad \text{(B3)}$$

allows to obtain an expression of porosity:

$$\phi = 1 - \frac{\rho_n^0\left(1-\phi_0\right)}{\rho_n} \qquad \text{(B4)}$$

with $C_0 = \rho_n^0\left(1-\phi_0\right)$ being a time integration constant. Substituting porosity into the total density, $\bar{\rho}$, (Equation (23)) allows $\bar{\rho}$ to be expressed with thermodynamically constrained fluid density, ρ_f, and density ratio, R, (Equation 6) as:

$$\bar{\rho} = \rho_f + R\rho_n^0\left(1-\phi_0\right) \quad \text{(B5)}$$

Using Equation (24) gives an equation relating $\bar{\rho}$ to the Darcy's flux:

$$\frac{d\bar{\rho}}{dt} = \nabla\cdot\left(\frac{\rho_f k}{\mu_f}\left(\nabla P_f + \rho_f g\right)\right) \quad \text{(B6)}$$

Finally, an expression using pressure time derivatives is obtained with Equation (B6) by using compressibilities:

$$\rho_f\beta_e\frac{dP_f}{dt} = \nabla\cdot\left(\frac{\rho_f k}{\mu_f}\left(\nabla P_f + \rho_f g\right)\right) \qquad \text{(B7)}$$

with

$$\beta_e = \beta_f + \beta_R \frac{(1-\phi_0)\rho_{n0}}{\rho_f} \qquad \text{(B8)}$$

Appendix C: Simplifications when assuming no fluid flow

In a closed system (no Darcy's flux)

$$\nabla\cdot\left(\phi\left(\overrightarrow{v_f} - \overrightarrow{v_s}\right)\right) = 0 \qquad \text{(C1)}$$

the equation for total mass conservation (Equation (24)) can be re-written as:

$$\nabla\cdot\overrightarrow{v_s} = -\frac{d\log\overline{\rho}}{dt} \qquad \text{(C2)}$$

Equation (4) reduces to:

$$\frac{d}{dt}\left(\frac{\overline{\rho}}{\rho_n(1-\phi)}\right) = 0 \qquad \text{(C3)}$$

which can be time integrated as

$$\frac{\overline{\rho}}{\rho_n(1-\phi)} = C_o = \frac{\overline{\rho}_0}{\rho_{n0}(1-\phi_0)} \qquad \text{(C4)}$$

to obtain an expression of porosity:

$$\phi = 1 - \frac{\rho_f}{C_o\rho_n + \rho_f - \rho_s} \qquad \text{(C5)}$$

that allows $\overline{\rho}$ to be expressed with thermodynamically constrained fluid density, ρ_f, and density ratio R (Equation 6) as:

$$\overline{\rho} = \frac{\rho_f C_o}{(C_o - R)} \qquad \text{(C6)}$$

Appendix D: Multiple volatile-bearing phases

The formalism used in section 4.4 with a unique hydrous phase only treats one (de)volatilization reaction. However, on a large pressure range, several volatilization and devolatilization reactions can occur. For example, when pressure increases in an ultramafic rock, three hydration and two dehydration reactions implying four hydrous phases (antigorite, talc, amphibole and chlorite) occur (Fig. A2). Moreover, hydrous phases contain strongly different amounts of water and have different densities. For example in mafic rocks, chlorite and amphibole, have average amounts of water of 11.3, and 2.1 *wt*.%, respectively, and average densities of 3,070, and 3,168 kg/m^3, respectively (Fig. A1).

This results in complex patterns in S_h, ρ_h and X_h which have to be modelled by decomposing the solid into several hydrous phases. We used a formalism to consider n volatile-bearing phases in the solid with different water content, X_i, and density, ρ_i, for each phase i. With this assumption, the volumetric proportion of volatile-bearing phases in the solid becomes

$$S_h = \sum_{i=1}^{n} S_i \qquad \text{(D1)}$$

or, by using Equation (42):

$$S_h = \sum_{i=1}^{n} \left(S_i^{max} - \left(S_i^{max} - S_i^{min} \right) \left(e^{-\beta_i \left(P_f - P_i \right)} \right) \right) \qquad \text{(D2)}$$

with P_i the pressure where S_i^{min} is reached for reaction i and S_i^{max} the maximum amount of hydrous phase i in the solid. Where reaction i does not occur (at $P_f < P_i$ for reaction with positive Clapeyron slope and at $P_f > P_i$ for reaction with negative Clapeyron slope), β_i is equal to zero. This formalism is found to reproduce accurately S_h evolution with pressure for ultramafic rocks (Fig. A2).

With this decomposition in phases, the parabolic equation for fluid pressure variations (Equation (21)) remains valid but the expression of β_e becomes

$$\beta_e = \beta_d - \beta_s' + \phi\beta_f + \frac{(1-\phi)\rho_a}{\rho_n}\sum_{i=1}^{n}\left(\left(S_i^{max} - S_i\right)\rho_i \Delta_{ri} V \beta_i\right) \qquad \text{(D3)}$$

with

$$\Delta_{ri} V = \frac{1-X_i}{\rho_a} - \frac{1}{\rho_i} + \frac{X_i}{\rho_f} + \sum_{i'=1;i'\neq i}^{n}\left(\frac{\rho_{i'} S_{i'}}{\rho_a \rho_f}\left(X_i - X_{i'}\right) - \frac{S_{i'}}{\rho_f}\left(X_i - \frac{\rho_{i'}}{\rho_i} X_{i'}\right)\right), \qquad \text{(D4)}$$

the change of volume for reaction of volatilization/devolatilization *i* which verifies the following property

$$\sum_{i=1}^{n}\left(\frac{S_i}{S_h}\rho_i \Delta_{ri} V\right) = \rho_h \Delta_r V \qquad \text{(D5)}$$

Acknowledgments

Discussions with J.A.D. Connolly and two anonymous reviewers helped to improve this manuscript. Electronic copies of the thermodynamic data shown in this article and used for numerical modelling are available from the authors on request at benjamin.malvoisin@gmail.com.

References

Aarnes, I., Y. Podladchikov, and H. Svensen (2012), Devolatilization-induced pressure build-up: Implications for reaction front movement and breccia pipe formation, *Geofluids*, *12*(4), 265–279, doi:10.1111/j.1468-8123.2012.00368.x.

Austrheim, H., and W. L. Griffin (1985), Shear deformation and eclogite formation within granulite-facies anorthosites of the bergen arcs, western norway, *Chemical Geology*, *50*(1), 267–281.

Balashov, V., and B. Yardley (1998), Modeling metamorphic fluid flow with reaction-compaction permeability feedbacks, *American Journal of Science*, *298*, 441–470.

Baumgartner, L., and J. Ferry (1991), A model for coupled fluid-flow and mixed-volatile mineral reactions with applications to regional metamorphism, *Contrib. Mineral. Petrol.*, *106*(3), 273–285, doi:10.1007/BF00324557.

Bruton, C. J., and H. C. Helgeson (1983), Calculation of the chemical and thermodynamic consequences of differences between fluid and geostatic pressure in hydrothermal systems.

Carlson, W. D. (2011), Porphyroblast crystallization: linking processes, kinetics, and microstructures, *International Geology Review*, *53*(3-4), 406–445, doi:10.1080/00206814.2010.496184.

Connolly, J. (2005), Computation of phase equilibria by linear programming: A tool for geodynamic modeling and its application to subduction zone decarbonation, *Earth and Planetary Science Letters*, *236*(1-2), 524–541.

Connolly, J., and Y. Podladchikov (1998), Compaction-driven fluid flow in viscoelastic rock, *Geodinamica Acta*, *11*(2-3), 55–84, doi:10.1016/S0985-3111(98)80006-5.

Connolly, J., and Y. Y. Podladchikov (2013), A hydromechanical model for lower crustal fluid flow, in *Metasomatism and the Chemical Transformation of Rock*, pp. 599–658, Springer.

Connolly, J. A. D. (1997), Devolatilization-generated fluid pressure and deformation-propagated fluid flow during prograde regional metamorphism, doi:10.1029/97JB00731.

Connolly, J. A. D. (2010), The mechanics of metamorphic fluid expulsion, *Elements*, *6*(3), 165–172, doi:10.2113/gselements.6.3.165.

Connolly, J. A. D., and Y. Y. Podladchikov (2007), Decompaction weakening and channeling instability in ductile porous media: Implications for asthenospheric

melt segregation, *Journal of Geophysical Research: Solid Earth*, *112*(10), doi:10.1029/2005JB004213.

Connolly, J. A. D., and Y. Y. Podladchikov (2015), An analytical solution for solitary porosity waves: dynamic permeability and fluidization of nonlinear viscous and viscoplastic rock, *Geofluids*, *15*(1-2), 269–292, doi:10.1111/gfl.12110.

Dahlen, F. (1992), Metamorphism of nonhydrostatically stressed rocks, *American Journal of Science*, *292*(3), 184–198.

Dale, J., R. Powell, R. White, F. Elmer, and T. Holland (2005), A thermodynamic model for ca–na clinoamphiboles in na2o–cao–feo–mgo–al2o3–sio2–h2o–o for petrological calculations, *Journal of Metamorphic Geology*, *23*(8), 771–791.

Duesterhoeft, E., J. Quinteros, R. Oberhänsli, R. Bousquet, and C. de Capitani (2014), Relative impact of mantle densification and eclogitization of slabs on subduction dynamics: A numerical thermodynamic/thermokinematic investigation of metamorphic density evolution, *Tectonophysics*, *637*, 20–29.

Fletcher, R. C., and E. Merino (2001), Mineral growth in rocks: Kinetic-rheological models of replacement, vein formation, and syntectonic crystallization, *Geochimica et Cosmochimica Acta*, *65*(21), 3733–3748, doi:10.1016/S0016-7037(01)00726-8.

Frantz, J., and H. Mao (1976), Bimetasomatism resulting from intergranular diffusion 1. Theoretical model for monomineralic reaction zone sequences, *Am. J. Sci.*, *276*(7), 817–840.

Galvez, M. E., C. E. Manning, J. A. Connolly, and D. Rumble (2015), The solubility of rocks in metamorphic fluids: A model for rock-dominated conditions to upper mantle pressure and temperature, *Earth and Planetary Science Letters*, *430*, 486–498.

Green, E., T. Holland, and R. Powell (2007), An order-disorder model for omphacitic pyroxenes in the system jadeite-diopside-hedenbergite-acmite, with applications to eclogitic rocks, *American Mineralogist*, *92*(7), 1181–1189.

Guy, B. (1993), Mathematical Revision of Korzhinskii Theory of Infiltration Metasomatic Zoning, *European Journal of Mineralogy*, *5*(2), 317–339.

Hacker, B. R. (2003), Subduction factory 1. Theoretical mineralogy, densities, seismic wave speeds, and H 2 O contents, *Journal of Geophysical Research*, *108*(B1), 1–26, doi:10.1029/2001JB001127.

Helgeson, H. C., D. H. Kirkham, and G. C. Flowers (1981), Theoretical prediction of the thermodynamic behavior of aqueous electrolytes by high pressures and temperatures; iv, calculation of activity coefficients, osmotic coefficients, and apparent molal and standard and relative partial molal properties to 600 degrees c and 5kb, *American Journal of Science*, *281*(10), 1249–1516.

Hesse, M., A. Schiemenz, Y. Liang, and E. Parmentier (2011), Compaction-dissolution waves in an upwelling mantle column, *Geophysical Journal International*, *187*(3), 1057–1075.

Hetényi, G. (2014), To conserve or not to conserve mass in numerical models, *Terra Nova*, pp. n/a–n/a, doi:10.1111/ter.12109.

Hetényi, G., V. Godard, R. Cattin, and J. a. D. Connolly (2011), Incorporating metamorphism in geodynamic models: The mass conservation problem, *Geophysical Journal International*, *186*(1), 6–10, doi:10.1111/j.1365-246X.2011.05052.x.

Hirt, C. (1968), Heuristic stability theory for finite-difference equations, *Journal of Computational Physics*, *2*(4), 339–355.

Hofmann, a. (1972), Chromatographic theory of infiltration metasomatism and its application to feldspars, doi:10.2475/ajs.272.1.69.

Holdaway, M. J., and J. W. Goodge (1990), Rock pressure vs. fluid pressure as a controlling influence on mineral stability: an example from New Mexico, *American Mineralogist*, *75*(9-10), 1043–1058.

Holland, T., and R. Powell (1996), Thermodynamics of order-disorder in minerals: I. Symmetric formalism applied to minerals of fixed composition, *American Mineralogist*, *81*(11-12), 1413–1424.

Holland, T., and R. Powell (2003), Activity–composition relations for phases in petrological calculations: an asymmetric multicomponent formulation, *Contributions to Mineralogy and Petrology*, *145*(4), 492–501.

Holland, T., J. Baker, and R. Powell (1998), Mixing properties and activity-composition relationships of chlorites in the system mgo-feo-al2o3-sio2-h2o, *European Journal of Mineralogy*, pp. 395–406.

Holland, T. J. B., and R. Powell (1998), An internally consistent thermodynamic data set for phases of petrological interest, *Journal of Metamorphic Geology*, *16*(3), 309–343, doi:10.1111/j.1525-1314.1998.00140.x.

Jamtveit, B., C. V. Putnis, and A. Malthe-Sørenssen (2009), Reaction induced fracturing during replacement processes, *Contributions to Mineralogy and Petrology*, *157*(1), 127–133.

Johnson, J. W., E. H. Oelkers, and H. C. Helgeson (1992), Supcrt92: A software package for calculating the standard molal thermodynamic properties of minerals, gases, aqueous species, and reactions from 1 to 5000 bar and 0 to 1000 c, *Computers & Geosciences*, *18*(7), 899–947.

Katz, R. F., M. G. Knepley, B. Smith, M. Spiegelman, and E. T. Coon (2007), Numerical simulation of geodynamic processes with the Portable Extensible Toolkit for Scientific Computation, *Physics of the Earth and Planetary Interiors*, *163*(1-4), 52–68, doi:10.1016/j.pepi.2007.04.016.

Kelemen, P. B., and G. Hirth (2012), Reaction-driven cracking during retrograde metamorphism: Olivine hydration and carbonation, *Earth and Planetary Science Letters*, *345-348*, 81–89, doi:10.1016/j.epsl.2012.06.018.

Keller, T., D. A. May, and B. J. P. Kaus (2013), Numerical modelling of magma dynamics coupled to tectonic deformation of lithosphere and crust, *Geophysical Journal International*, pp. 1–37.

Korzhinskii, D. (1970), Theory of metasomatic zoning: Oxford univ, *Press, London*.

Kulik, D. A., T. Wagner, S. V. Dmytrieva, G. Kosakowski, F. F. Hingerl, K. V. Chudnenko, and U. R. Berner (2013), Gem-selektor geochemical modeling package: revised algorithm and gems3k numerical kernel for coupled simulation codes, *Computational Geosciences*, *17*(1), 1–24.

Liang, Y., A. Schiemenz, M. A. Hesse, and E. Parmentier (2011), Waves, channels, and the preservation of chemical heterogeneities during melt migration in the mantle, *Geophysical Research Letters*, *38*(20).

Lichtner, P., and Q. Kang (2007), Upscaling pore-scale reactive transport equations using a multiscale continuum formulation, American Geophysical Union, doi:10.1029/2006WR005664.

Lichtner, P. C., and J. W. Carey (2006), Incorporating solid solutions in reactive transport equations using a kinetic discrete-composition approach, *Geochimica et Cosmochimica Acta*, *70*(6), 1356–1378, doi:10.1016/j.gca.2005.11.028.

Lichtner, P. C., H. C. Helgeson, and W. M. Murphy (1987), Lagrangian and eularian representations of metasomatic alteration of minerals, in *Chemical Transport in Metasomatic Processes*, edited by H. C. Helgeson, pp. 519–545, D. Reidel Publishing Company, Dordrecht.

Llana-Fúnez, S., J. Wheeler, and D. R. Faulkner (2012), Metamorphic reaction rate controlled by fluid pressure not confining pressure: Implications of dehydration experiments with gypsum, *Contributions to Mineralogy and Petrology*, *164*(1), 69–79, doi:10.1007/s00410-012-0726-8.

Mantegazzi, D., C. Sanchez-Valle, and T. Driesner (2013), Thermodynamic properties of aqueous NaCl solutions to 1073K and 4.5GPa, and implications for dehydration reactions in subducting slabs, *Geochimica et Cosmochimica Acta*, *121*, 263–290, doi:10.1016/j.gca.2013.07.015.

McKenzie, D. (1984), The generation and compaction of partially molten rock, *Journal of Petrology*, *25*(3), 713–765.

Navon, O., and E. Stolper (1987), Geochemical consequences of melt percolation: the upper mantle as a chromatographic column, *The Journal of Geology*, pp. 285–307.

Newton, R., T. Charlu, and O. Kleppa (1980), Thermochemistry of the high structural state plagioclases, *Geochimica et Cosmochimica Acta*, *44*(7), 933–941.

Padrón-Navarta, J. A., V. L. Sánchez-Vizcaíno, J. Hermann, J. a. D. Connolly, C. J. Garrido, M. T. Gómez-Pugnaire, and C. Marchesi (2013), Tschermak's substitution in antigorite and consequences for phase relations and water liberation in high-grade serpentinites, *Lithos*, *178*, 186–196, doi:10.1016/j.lithos.2013.02.001.

Plank, T., and C. H. Langmuir (1998), The chemical composition of subducting sediment and its consequences for the crust and mantle, *Chemical Geology*, *145*(3-4), 325–394, doi:10.1016/S0009-2541(97)00150-2.

Plümper, O., A. Røyne, A. Magrasó, and B. Jamtveit (2012), The interface-scale mechanism of reaction-induced fracturing during serpentinization, *Geology*, *40*(12), 1103–1106.

Putnis, A., and C. V. Putnis (2007), The mechanism of reequilibration of solids in the presence of a fluid phase, *Journal of Solid State Chemistry*, *180*(5), 1783–1786, doi:10.1016/j.jssc.2007.03.023.

Richter, F. M., and D. McKenzie (1984), Dynamical models for melt segregation from a deformable matrix, *The Journal of Geology*, pp. 729–740.

Scherer, G. W. (2004), Stress from crystallization of salt, *Cement and Concrete Research*, *34*(9), 1613–1624, doi:10.1016/j.cemconres.2003.12.034.

Schmidt, M. W., and S. Poli (1998), Experimentally based water budgets for dehydrating slabs and consequences for arc magma generation, *Earth and Planetary Science Letters*, *163*(1-4), 361–379, doi:10.1016/S0012-821X(98)00142-3.

Scott, D. R., and D. J. Stevenson (1986), Magma ascent by porous flow, *Journal of Geophysical Research B*, *91*(B9), 9283–9296.

Sedqui, A., and B. Guy (2001), Échange chromatographique de deux constituants indépendants entre un fluide aqueux et une solution solide à trois pôles; application à la substitution ca–fe–mn des grenats de skarn, *Comptes Rendus de l'Académie des Sciences-Series IIA-Earth and Planetary Science*, *332*(4), 227–234.

Spiegelman, M., P. B. Kelemen, and E. Aharonov (2001), Causes and consequences of flow organization during melt transport: The reaction infiltration instability in compactible media, *J. geophys. Res*, *106*(B2), 2061–2077.

Staudigel, H., T. Plank, B. White, and H.-U. Schmincke (1996), Geochemical fluxes during seafloor alteration of the basaltic upper oceanic crust: Dsdp sites 417 and 418, *Subduction top to bottom*, pp. 19–38.

Steefel, C. I., D. J. DePaolo, and P. C. Lichtner (2005), Reactive transport modeling: An essential tool and a new research approach for the Earth sciences, *Earth and Planetary Science Letters*, *240*(34), 539–558, doi:10.1016/j.epsl.2005.09.017.

Sverjensky, D. a., B. Harrison, and D. Azzolini (2014), Water in the deep Earth: The dielectric constant and the solubilities of quartz and corundum to 60kb and 1200??C, *Geochimica et Cosmochimica Acta*, *129*, 125–145, doi:10.1016/j.gca.2013.12.019.

Tajčmanová, L., Y. Podladchikov, R. Powell, E. Moulas, J. C. Vrijmoed, and J. a. D. Connolly (2014), Grain-scale pressure variations and chemical equilibrium in high-grade metamorphic rocks, *Journal of Metamorphic Geology*, *32*(2), 195–207, doi:10.1111/jmg.12066.

Thompson, J. B. (1970), Geochemical reaction and open systems, *Geochimica et Cosmochimica Acta*, *34*(5), 529–551.

Tian, M., and J. J. Ague (2014), The impact of porosity waves on crustal reaction progress and co 2 mass transfer, *Earth and Planetary Science Letters*, *390*, 80–92.

Tirone, M., J. Ganguly, and J. P. Morgan (2009), Modeling petrological geodynamics in the Earth's mantle, *Geochemistry, Geophysics, Geosystems*, *10*(4), doi:10.1029/2008GC002168.

Turcotte, D. L., and G. Schubert (2014), *Geodynamics*, Cambridge University Press.

Waldbaum, D., and J. Thompson (1968), Mixing properties of sanidine crystalline solutions.2. calculations based on volume data., *American Mineralogist*, *53*, 2000–2017.

White, R., R. Powell, T. Holland, and B. Worley (2000), The effect of tio˜ 2 and fe˜ 2o˜ 3 on metapelitic assemblages at greenschist and amphibolite facies conditions: mineral equilibria calculations in the system k˜ 2o-feo-mgo-al˜ 2o˜ 3-sio˜ 2-h˜ 2o-tio˜ 2-fe˜ 2o˜ 3, *Journal of Metamorphic Geology*, *18*(5), 497–512.

Wiggins, C., and M. Spiegelman (1995), Magma migration and magmatic solitary waves in 3-d, *Geophysical Research Letters*, *22*(10), 1289–1292.

Wilson, C. R., M. Spiegelman, P. E. van Keken, and B. R. Hacker (2014), Fluid flow in subduction zones: The role of solid rheology and compaction pressure, *Earth and Planetary Science Letters*, *401*, 261–274, doi:10.1016/j.epsl.2014.05.052.

Xu, T., E. Sonnenthal, N. Spycher, and K. Pruess (2006), TOUGHREACT - A simulation program for non-isothermal multiphase reactive geochemical transport in variably saturated geologic media: Applications to geothermal injectivity and CO2 geological sequestration, *Computers and Geosciences*, *32*(2), 145–165, doi:10.1016/j.cageo.2005.06.014.

Yarushina, V. M., and Y. Y. Podladchikov (2015), (de)compaction of porous viscoelastoplastic media: Model formulation, *Journal of Geophysical Research: Solid Earth*, pp. n/a–n/a, doi:10.1002/2014JB011258, 2014JB011258.

Figure 1 Non-volatile species density (ρ_n; A, C and E) and density ratio (R; B, D and F) as a function of pressure and temperature for three univariant reactions. A and B: antigorite dehydration. C and D: muscovite dehydration. E and F: calcite

decarbonation. Pseudosection diagrams are displayed on A, C and E for each reaction. Calculations were performed with Perple_X [Connolly, 2009] and the database of *Holland et al.* [1998]. Note the abrupt change of ρ_n and R along the reaction line.

Figure 2 Fluid density (ρ_f) as a function of pressure and temperature for ultramafic and mafic rocks (A) and for sedimentary rocks (B). The field where water is present in A is delimited with a blue line for ultramafic rocks and with a black line for mafic rocks. Note the continuous variation of ρ_f with pressure which can be fitted by using an exponential law with β_f as a parameter (Equation (18)).

Figure 3 Variation of the non-volatile species density (ρ_n; A, C and E) and of the density ratio (R; B, D and F) for system compositions of ultramafic rocks (A and B), mafic rocks (C and D) and sedimentary rocks (E and F). Pseudosection diagrams are displayed in white on A, C and E with the mineralogical assemblage corresponding to each number on the right.

Figure 4 Position in the P-T space of a dehydration reaction having a positive Clapeyron slope at low pressure and a negative Clapeyron slope at high pressure. Note that the change in volume with pressure is negative for reactions with both positive and negative Clapeyron slopes and, using Equation (33), β_R is thus always positive. In the case of solid decomposition in phases (section 4.4), note also that for both negative and positive Clapeyron slopes, β_h (defined in Equation (42)) and the volume change of reaction ($\Delta_r V$, defined in Equation (44)) have the same sign. For positive Clapeyron slope, the change in volume ($\Delta_r V$) and β_h are both positive whereas, for negative Clapeyron slopes, they are both negative. As a result, the effective compressibility is always positive in Equation (22) and in Equation (45) and Equation (21) can be solved without generating instabilities.

Figure 5 A: Change of volume during antigorite dehydration (Δ_{rV}) calculated with Perple_X (plain line) and with Equation (35) (dashed line). B: comparison of the

Clapeyron slope calculated with Perple_X ($\frac{dT}{dP}$; plain line) with $\frac{\Delta_r V}{\Delta_r S}$ calculated with Equation (35) for Δ_{rV} and Δ_{rS} computed with Perple_X (dashed line). Note the good match between the various expressions.

Figure 6 Comparison between bulk and phases properties for ultramafic rocks (the same properties for mafic and sedimentary rocks can be found in Supplementary figures S3 and S4). Labels for the superimposed pseudosection diagram in A are displayed on Figure 3. A: mass fraction of water in the rock (X_s). B: Mass fraction of water in antigorite (X_h). C: solid density (ρ_s). D: hydrous phases density (ρ_h). E: anhydrous phases density (ρ_a).

Figure 7 Volume fraction of hydrous phases in the solid (S_h) as a function of the fluid pressure (P_f) minus the pressure of the reaction (P_r) for both olivine hydration (A) and antigorite dehydration (B). Each black line corresponds to S_h for a temperature fixed between $400\,^{\circ}C$ and $463\,^{\circ}C$ for olivine hydration and between $631\,^{\circ}C$ and $635\,^{\circ}C$ for antigorite dehydration. The blue lines are fits of the black lines with the exponential law of Equation (42).

Figure 8 Mass fraction of water in the solid (X_s; A, E and I), fluid density (ρ_f; B, F and J), non-volatile species density (ρ_n; C, G and K) and density ratio (R; D, H and L) for selected P-T domains with compositions of ultramafic rocks (A, B, C and D), mafic rocks (E, F, G and H) and sedimentary rocks (I, J, K and L). In these domains, the reactions of antigorite and chlorite dehydration and carbonate decarbonation occur for ultramafic, mafic and sedimentary rocks compositions, respectively. The data computed along the black lines were used in numerical modelling and either fitted for R in the case of ultramafic rocks composition and fluid densities or used in look-up tables for ρ_n and R in the case of mafic rocks and sedimentary rocks composition.

Figure 9 One-dimensional numerical modelling of the relaxation in space of a pressure increase for three cases using the parameters for antigorite (A, B, C

and D) and chlorite (E, F, G and H) dehydrations and carbonate decarbonation (I, J, K and L) given in Figure 8. Initial conditions (dashed lines) and results after simulation durations of 1 s for antigorite dehydration and 300 s for chlorite dehydration and carbonate decarbonation (plain lines) are both shown. Results for the reacting porosity waves model (black lines) and a non-reactive model (green lines) are both shown. For antigorite dehydration, results for two reacting porosity waves models are shown in which R variations are either approximated with a fit of the data (red line) or calculated with look-up tables (black line). A, E and I: pressure profile. B, F and J: porosity profile. C, G and K: phases modes for initial conditions. D, H and L: phases modes after the simulation durations given above. Note that the shape of the profiles depends on the Clapeyron slope of the reaction. As porosity increases with pressure for negative Clapeyron slopes (A, B, C and D), fluid propagates faster in the center of the model than on the sides and sharp profiles are obtained. For positive Clapeyron slopes (E, F, G and H and I, J, K and L) an opposite trend is observed with smoother pressure and porosity variations due the decrease of porosity with pressure.

Figure 10 Pressure (A, C, E and G) and porosity (B, D, F and H) changes as a function of time for the relaxation of an initial positive (A, B, E and F) or negative (C, D, G and H) pressure anomaly. Reactions having negative (A, B, C and D) and positive (E, F, G and H) Clapeyron slopes were both investigated by using the parameters derived for antigorite and chlorite dehydrations shown in Figure 8, respectively. Note that sharp pressure and porosity anomalies propagate for negative Clapeyron slope and positive pressure pulse at the center of the model (A and B) and for positive Clapeyron slopes and negative pressure pulse at the center of the model (G and H). This is due to significant porosity and permeability increases at the center of these models which allow faster propagation of the fluid than on the both sides of the model. An opposite trend with smooth pressure and porosity profiles is obtained in Figures C, D, E and F.

Figure 11 Comparison of one dimensional models of fluid flow with or without considering the impact of elastic deformation and antigorite (A and B; negative Clapeyron slope) or chlorite dehydration (C and D; positive Clapeyron slope). The profiles are displayed after a simulation time of 1.64 s for antigorite dehydration and 190 s for chlorite dehydration. A and C: evolution of fluid pressure. B and D: evolution of porosity. E: evolution of ρ_n with the fluid pressure for chlorite dehydration. The various parameters used for the different models are given on the figure. For negative Clapeyron slope (A and B), reaction and elastic deformation have similar effects on the porosity which increases with the fluid pressure. This results in a faster propagation of the porosity front as reaction and deformation are both considered (blue and green lines compared to red and cyan lines, respectively). For positive Clapeyron slope, reaction and elastic deformation have opposite effects on porosity variation which decreases due to reaction and increases due to deformation when fluid pressure increases. This results in different shapes of the pressure and porosity profiles for different values of $\beta_d - \beta_s^{'}$. For conditions where the impact of reaction and deformation are equivalent $\beta_d - \beta_s^{'} = 0.07 GPa^{-1}$, the shape of the profile is controlled by the variation of ρ_n with fluid pressure following Equation (11). The competition between deformation and reaction also induces a slower propagation of the porosity front.

Figure A1 Density (A and C) and mass fraction of water (B and D) in chlorite (A and B) and amphibole (C and D) formed in mafic rocks.

Figure A2 A: variations of the volume fraction of hydrous phases in the solid (S_h) as a function of pressure along a profile calculated with ultramafic rocks composition at a fixed temperature of $625^{\circ}C$. The blue line corresponds to the data calculated with Perple_X and the red line to a fit obtained with Equation (D2). B: phase modes along the profile. As pressure increases, three increases in S_h occur first during amphibole + talc + chlorite formation, then during chlorite and talc reaction to form antigorite and finally during amphibole hydration to form

antigorite and clinopyroxene. At pressure above 3.5 GPa S_h decreases first through antigorite dehydration to form olivine, orthopyroxene and chlorite and then through chlorite dehydration to form olivine and garnet.

Table 1 Symbols used in the mathematical model

Symbol	Definition	Unit
P_f	Fluid pressure	*Pa*
P_r	Pressure of the reaction	*Pa*
P_i	Pressure of reaction *i* when multiple reactions are considered	*Pa*
$\overline{P}$	Lithostatic pressure	*Pa*
P_s	Solid pressure	*Pa*
T	Temperature	*K*
$\overrightarrow{v_s}$	Solid velocity	$m.s^{-1}$
$\overrightarrow{v_f}$	Fluid velocity	$m.s^{-1}$
X_h	Mass fraction of fluid in hydrous solid	*wt.*%
X_i	Mass fraction of fluid in hydrous phase *i*	*wt.*%
X_s	Mass fraction of fluid in solid	*wt.*%
R	density ratio	*none*
ϕ	Porosity, fluid volume fraction	*none*
ϕ_0	Porosity before reaction	*none*
ρ_f	Fluid density	$kg.m^{-3}$
ρ_s	Solid density	$kg.m^{-3}$
ρ_n	Density of the non-volatile species	$kg.m^{-3}$
ρ_n^0	Density of the non-volatile species before reaction	$kg.m^{-3}$
$\overline{\rho}$	Total density	$kg.m^{-3}$
$\overline{\rho}_0$	Total density before reaction	$kg.m^{-3}$
ρ_h	Hydrous solid density	$kg.m^{-3}$
ρ_i	Density of hydrous solid *i*	$kg.m^{-3}$
ρ_a	Anhydrous solid density	$kg.m^{-3}$
V	Volume of the system	m^3
$\Delta_r V$	Volume change during the reaction	m^3
$\Delta_{ri} V$	Volume change during reaction *i*	m^3

Symbol	Definition	Unit
$\Delta_r S$	Entropy change during the reaction	$J.K^{-1}$
$\Delta_r P$	Pressure change during the reaction	Pa
C_0	Constant defined in Equation (25)	$kg.m^{-3}$
C_o	Constant defined in Equation (31)	*none*
k_0	Background permeability	m^2
η_ϕ	Pore viscosity	$Pa.s$
μ_f	Fluid viscosity	$Pa.s$
g	Gravity acceleration	$m^2.s^{-1}$
β_d	Drained compressibility	Pa^{-1}
β_s'	Solid compressibility measured in unjacketed tests	Pa^{-1}
β_s	Solid compressibility defined in equation (20)	Pa^{-1}
β_e	Effective compressibility	Pa^{-1}
β_R	Compressibility of R	Pa^{-1}
β_f	Fluid compressibility	Pa^{-1}
β_h	Solubility of the hydrous phase in the solid	Pa^{-1}
β_i	Solubility of the hydrous phase i	Pa^{-1}
S_h	Volume fraction of hydrous phases in the solid	*vol.*%
S_h^{max}	Maximum of S_h	*vol.*%
S_i	Volume fraction of the hydrous phases i in the solid	*vol.*%
S_i^{max}	Maximum of S_i	*vol.*%
$\vec{e}_z$	Unit vector along upward directed z-axis	*none*

Table 2 Rock compositions used for thermodynamic modelling.

Elements (*wt.*%)	Ultramafic rock	Mafic rock	Sedimentary rock
SiO_2	39.58	47.85	58.67
TiO_2	0	0	0.62
Al_2O_3	1.51	16.24	11.93
FeO	8.54	9.40	5.22
MnO	0	0	0.32
MgO	37.89	6.95	2.48
CaO	1.25	13.41	5.96

Elements (*wt.*%)	Ultramafic rock	Mafic rock	Sedimentary rock
Na_2O	0	2.15	2.43
K_2O	0	0	2.04
H_2O	11.24	4	7.30
CO_2	0	0	3.01
Total	100	100	100

Table 3 Solid solution models for the phases used in the Ultramafic (Ult), Mafic (Maf) and Sedimentary (Sed) compositions.

Solid solution model	Rock type	Formula	References
Antigorite (Atg)	Ult	$Mg_{x(48-y)}Fe_{(1-x)(48-y)}Al_{8y}Si_{34-y}O_{85}(OH)_{62}$	*Padrón-Navarta et al.* [2013]
Amphibole (Amp)	Ult, Maf, Sed	$Ca_{2(y+u+v)}Na_{u+2(w+z)}(Mg_xFe_{1-x})_{7-3u-2v-4(w+z)}$	
		$Fe^{3+}_{2z}Al_{4y+3v+2w}Si_{8-(y+v)}O_{22}(OH)_2$	*Dale et al.* [2005]
Brucite (Brc)	Ult	$Mg_xFe_{1-x}(OH)_2$	ideal
Chloritoid (Cld)	Maf, Sed	$Mg_xFe_yMn_{1-x-y}Al_2SiO_5(OH)_2$	*White et al.* [2000]
Chlorite (Chl)	Ult, Maf, Sed	$(Mg_xFe_wMn_{1-x-w})_{5-y+z}$	
		$Al_{2(1+y-z)}Si_{3-y+z}O_{10}(OH)_8$	*Holland et al.* [1998]
Cordierite (Crd)	Maf, Sed	$Mg_{2x}Fe_{2y}Mn_{2(1-x-y)}Al_4Si_5O_{18}\cdot(H_2O)_z$	ideal
Clinopyroxene (Cpx)	Ult	$Na_{1-y}Ca_yMg_{xy}Fe_{(1-x)y}Al_ySi_2O_6$	*Holland and Powell* [1996]
Dolomite (Dol)	Sed	$CaMg_xFe_{1-x}(CO_3)_2$	*Holland and Powell* [2003]
Epidote (Ep)	Maf, Sed	$Ca_2Al_{3-2x}Fe_{2x}Si_3O_{12}(OH)$	*Holland and Powell* [1998]
Garnet (Grt)	Ult, Maf, Sed	$(Fe_xCa_yMg_zMn_{1-x-y-z})_3(Fe_{1-w}Al_w)_2Si_3O_{12}$	*White et al.* [2000]
K-feldspar (Ksp)	Sed	$Na_xK_{1-x}AlSi_3O_8$	*Waldbaum and Thompson* [1968]
Olivine (Ol)	Ult	$Mg_{2x}Fe_{2y}Mn_{2(1-x-y)}SiO_4$	*Holland and Powell* [1998]
Omphacite (Omp)	Maf, Sed	$Na_{y+w}(CaMg_xFe^{2+}_{(1-x)})_{1-y-w}Al_yFe^{3+}_wSi_2O_6$	*Green et al.* [2007]
Orthopyroxene (Opx)	Ult	$(Mg_xFe_{1-x})_{2-y}Al_{2y}Si_{2-y}O_6$	*Holland and Powell* [1996]
Phengite (Ph)	Maf, Sed	$K_xNa_{1-x}Mg_yFe_zAl_{3-2(y+z)}Si_{3+y+z}O_{10}(OH)_2$	*Holland and Powell* [1998]
Plagioclase (Pl)	Maf, Sed	$Na_xCa_{1-x}Al_{2-x}Si_{2+x}O_8$	*Newton et al.* [1980]
Pumpellyite (Pmp)	Maf, Sed	$Ca_4(Mg_xFe_{1-x})_2Al_5Si_6O_{21}(OH)_7$	model from C. Mazzoli
Staurolite (St)	Maf, Sed	$Mg_{4x}Fe_{4y}Mn_{4(1-x-y)}Al_{18}Si_{7.5}O_{48}H_4$	*Holland and Powell* [1998]

Solid solution model	Rock type	Formula	References
Talc (Tlc)	Ult	$(Mg_xFe_{1-x})_{3-y}Al_{2y}Si_{4-y}O_{10}(OH)_2$	ideal
Ti-biotite (Bt)	Sed	$K(Mg_xFe_yMn_{1-x-y})_{3-w-z/2}Ti_z$ $Al_{1+2w}Si_{3-w}O_{10}(OH)_2$	*White et al.* [2000]

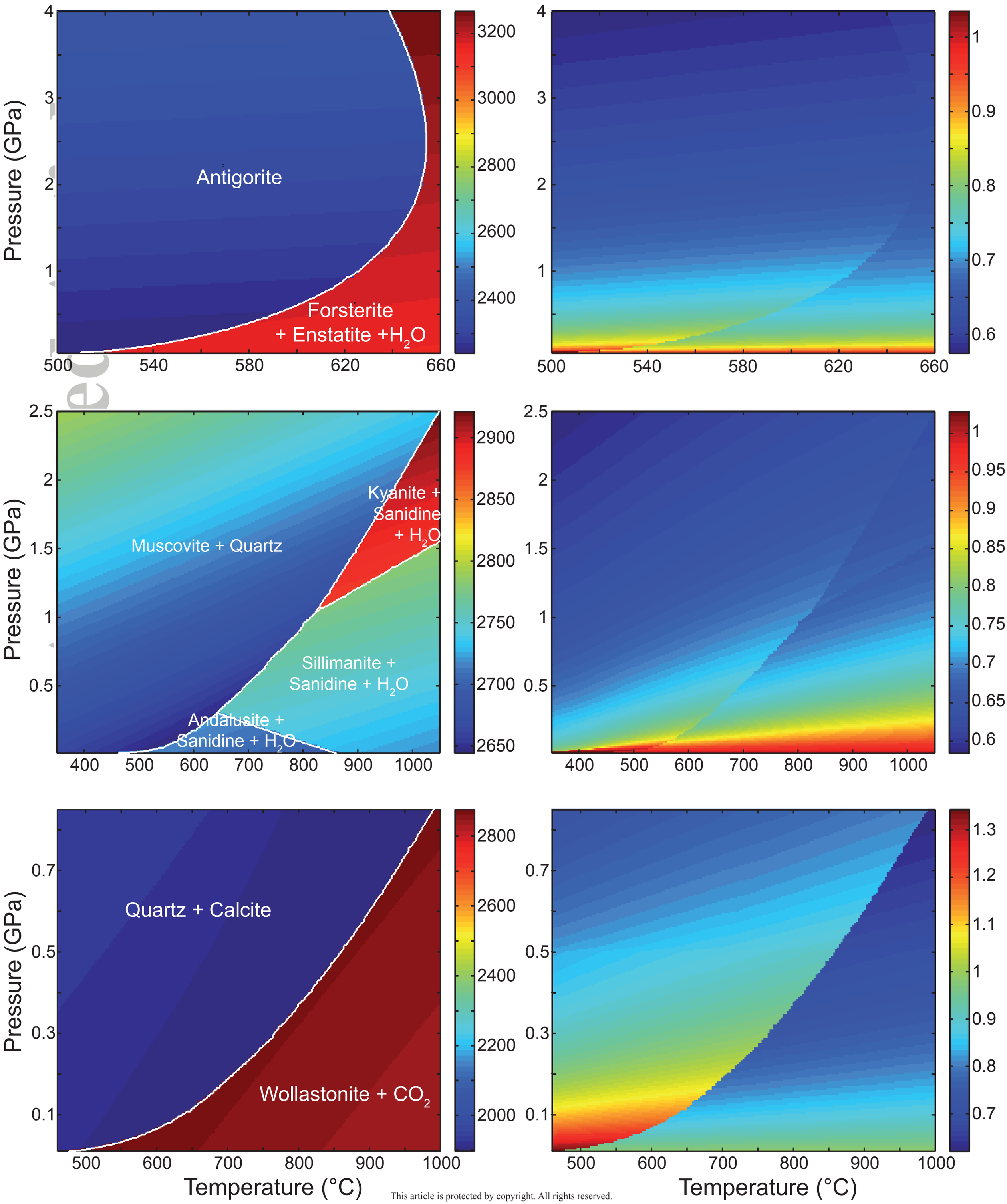

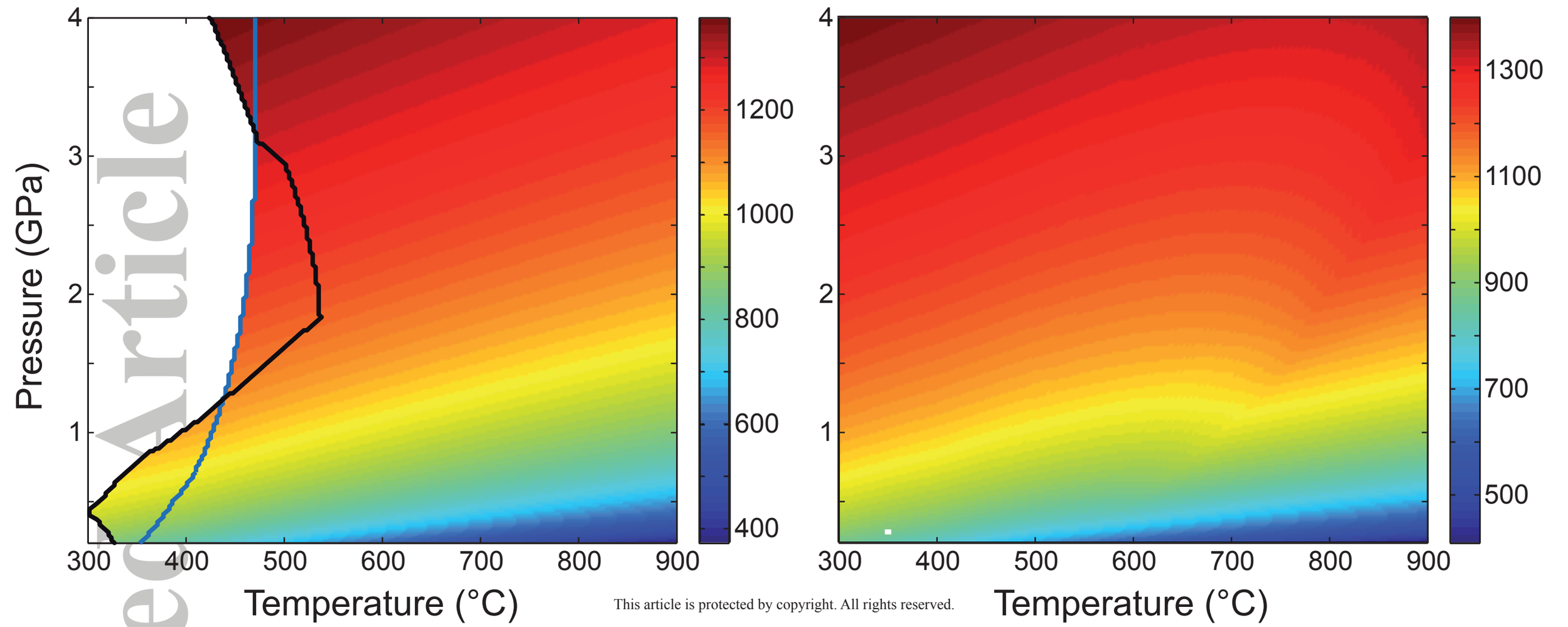

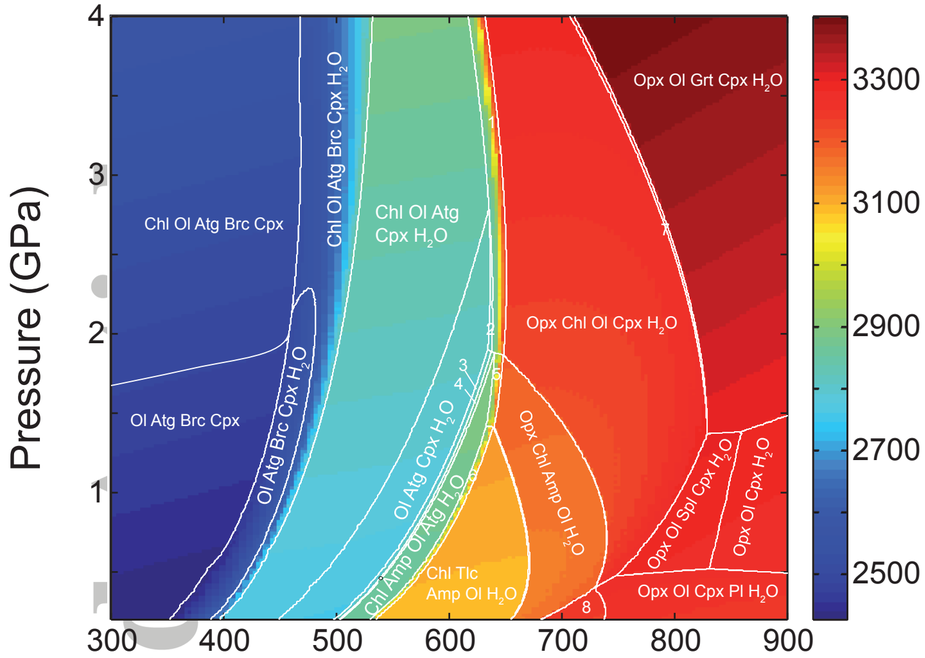

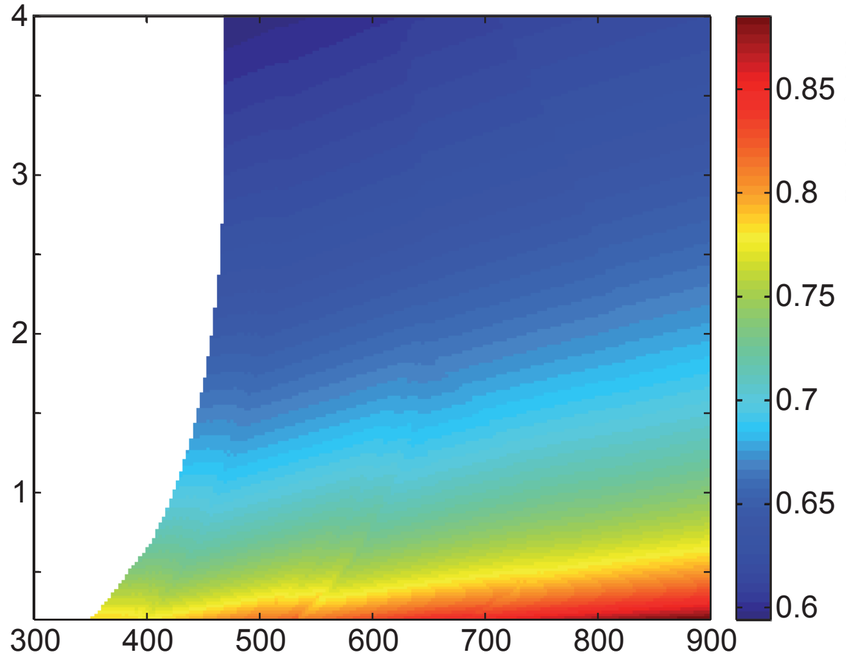

1 : Opx Chl Ol Atg Cpx H_2O
2 : Opx Ol Atg Cpx H_2O
3 : Opx Amp Ol Atg Cpx H_2O
4: Chl Amp Ol Atg Cpx H_2O
5: Opx Chl Amp Ol Atg H_2O
6: Chl Tlc Amp Ol Atg H_2O
7: Opx Chl Ol Grt Cpx H_2O
8: Opx Amp Ol Pl H_2O

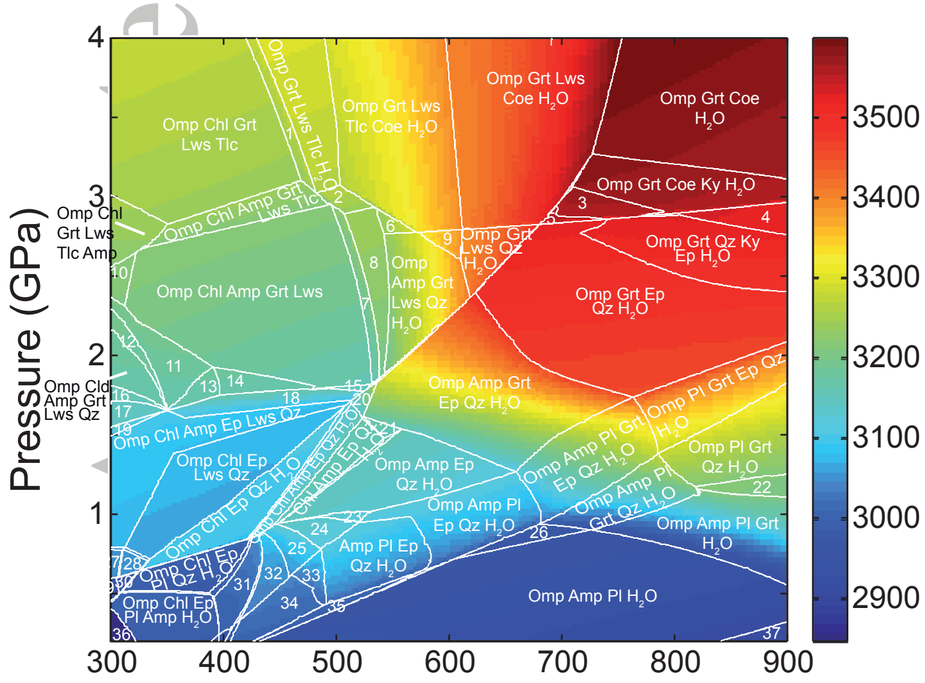

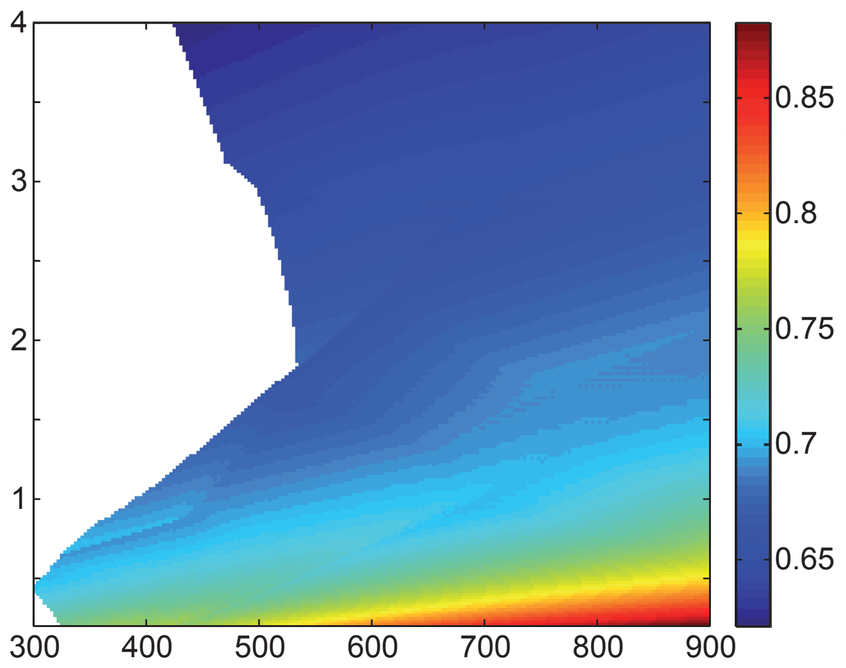

1: Omp Chl Grt Lws Tlc H_2O
2: Omp Amp Grt Lws Tlc H_2O
3: Omp Grt Coe Ky Ep H_2O
4: Omp Grt Qz Ky H_2O
5: Omp Grt Ep Coe H_2O
6: Omp Amp Grt Lws Coe H_2O
7: Omp Chl Amp Grt Lws H_2O
8: Omp Amp Grt Lws H_2O
9: Omp Grt Lws Tlc Qz H_2O
10: Omp Chl Amp Grt Lws Tlc
11: Omp Chl Cld Amp Grt Lws
12: Omp Cld Amp Grt Lws
13: Omp Chl Cld Amp Grt Lws Qz
14: Omp Chl Amp Grt Lws Qz
15: Omp Chl Amp Grt Ep Lws
16: Omp Cld Amp Grt Ep Lws
17: Omp Chl Cld Amp Ep Lws
18: Omp Chl Amp Grt Ep Lws Qz
19: Omp Chl Amp Ep Lws Qz
20: Omp Chl Amp Grt Ep Qz H_2O
21: Amp Grt Ep Qz H_2O
22: Omp Pl Grt H_2O
23: Omp Amp Ep Pl Qz H_2O
24: Amp Ep Pl Qz H_2O
25: Chl Amp Ep Pl Qz H_2O
26: Omp Amp Pl Qz H_2O
27: Omp Chl Ep Pmp Qz Amp
28: Omp Chl Ep Pmp Qz
29: Omp Chl Ep Pmp Pl Qz Amp
30: Omp Chl Ep Pmp Pl Qz
31: Omp Chl Ep Prh Pl Amp H_2O
32: Chl Amp Ep Pl H_2O
33: Chl Amp Pl Ep Qz H_2O
34: Chl Amp Pl Ep H_2O
35: Amp Pl Ep H_2O
36: Omp Chl Ep Prh Pl Amp
37: Omp Amp Pl Fa H_2O

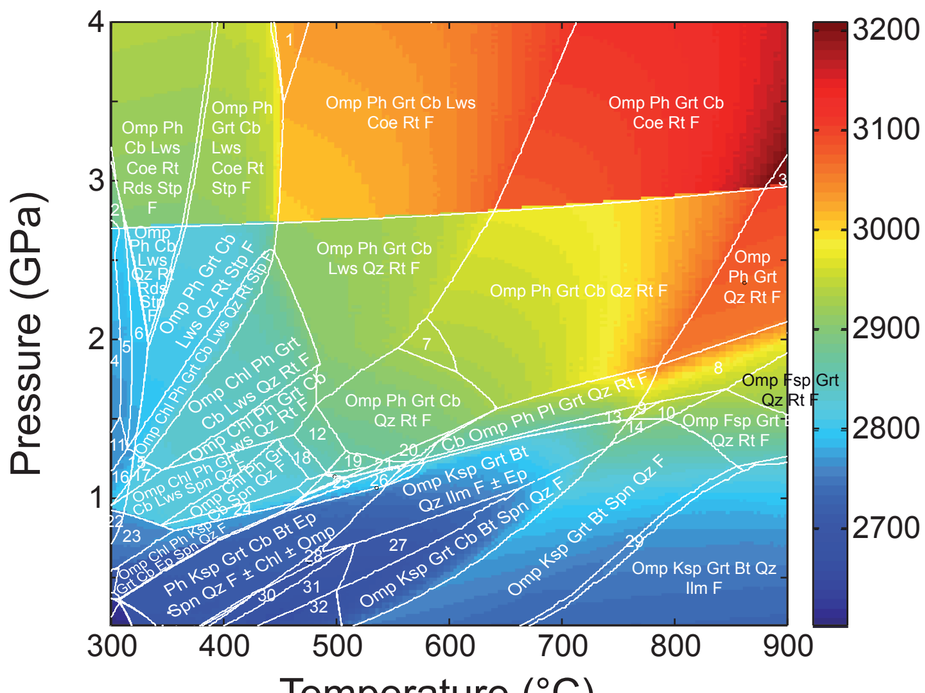

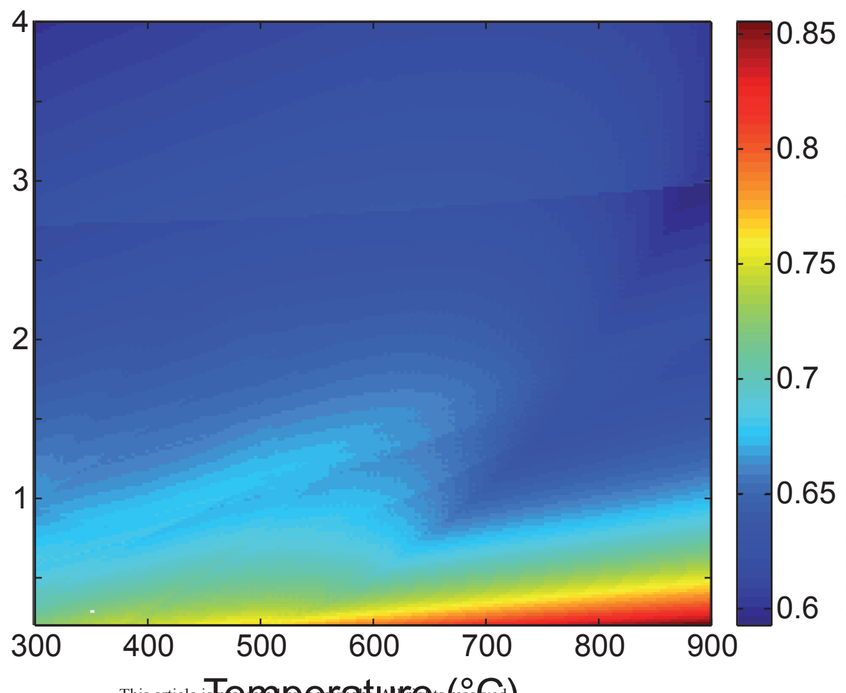

1: Omp Ph Grt CbLws Coe Rt Sd F
2: Omp Ph Cb Lws Spn Coe Rt Stp F
3: Omp Ph Grt Coe Rt F
4: Omp Ph Cb Lws Spn Qz Stp F
5: Omp Ph Cb Lws Spn Qz Rt Stp F
6: Omp Ph Cb Lws Qz Rt Stp F
7: Omp Ph Grt Cb Ep Qz Rt F
8: Omp Ph Fsp Grt Qz Rt F
9: Omp Ph Pl Grt Bt Qz Rt F
10: Omp Ph Fsp Grt Bt Qz Rt F
11: Amp Omp Ph Cb Lws Spn Qz Stp F
12: Omp Chl Ph Grt Cb Qz Rt F
13: Omp Ph Pl Grt Cb Bt Qz Rt F
14: Omp Ph Fsp Grt Bt Spn Qz F
15: Omp Chl Ph Grt Cb Lws Spn Qz Stp F
16: Omp Chl Ph Cb Lws Spn Qz Stp F
17: Omp Chl Ph Grt Cb Lws Spn Qz F
18: Omp Chl Ph Grt Cb Spn Qz Rt F
19: Omp Ph Amp Grt Cb Qz Rt F
20: Cb Omp Ph Ksp Grt Qz Rt F
21: Omp Ph Amp Ksp Grt Cb Qz Rt F
22: Omp Chl Ph Ksp Cb Lws Spn Qz Stp F
23: Omp Chl Ph Ksp Grt Cb Lws Spn Qz F
24: Omp Chl Ph Ksp Grt Cb Spn Qz F
25: Omp Ph Amp Ksp Grt Cb Spn Qz F
26: Omp Ph Amp Ksp Grt Cb Ep Spn Qz F
27: Omp Ksp Grt Cb Bt Ep Spn Qz F
28: Ph Ksp Grt Cb Bt Ep Spn Qz F
29: Omp Ksp Grt Bt Spn Qz Ilm F
30: Ksp Grt Cb Bt Ep Spn Qz F
31: Omp Ksp Grt Cb Bt Ep Spn Qz F
32: Omp Ksp Grt Cb Bt Spn Qz F

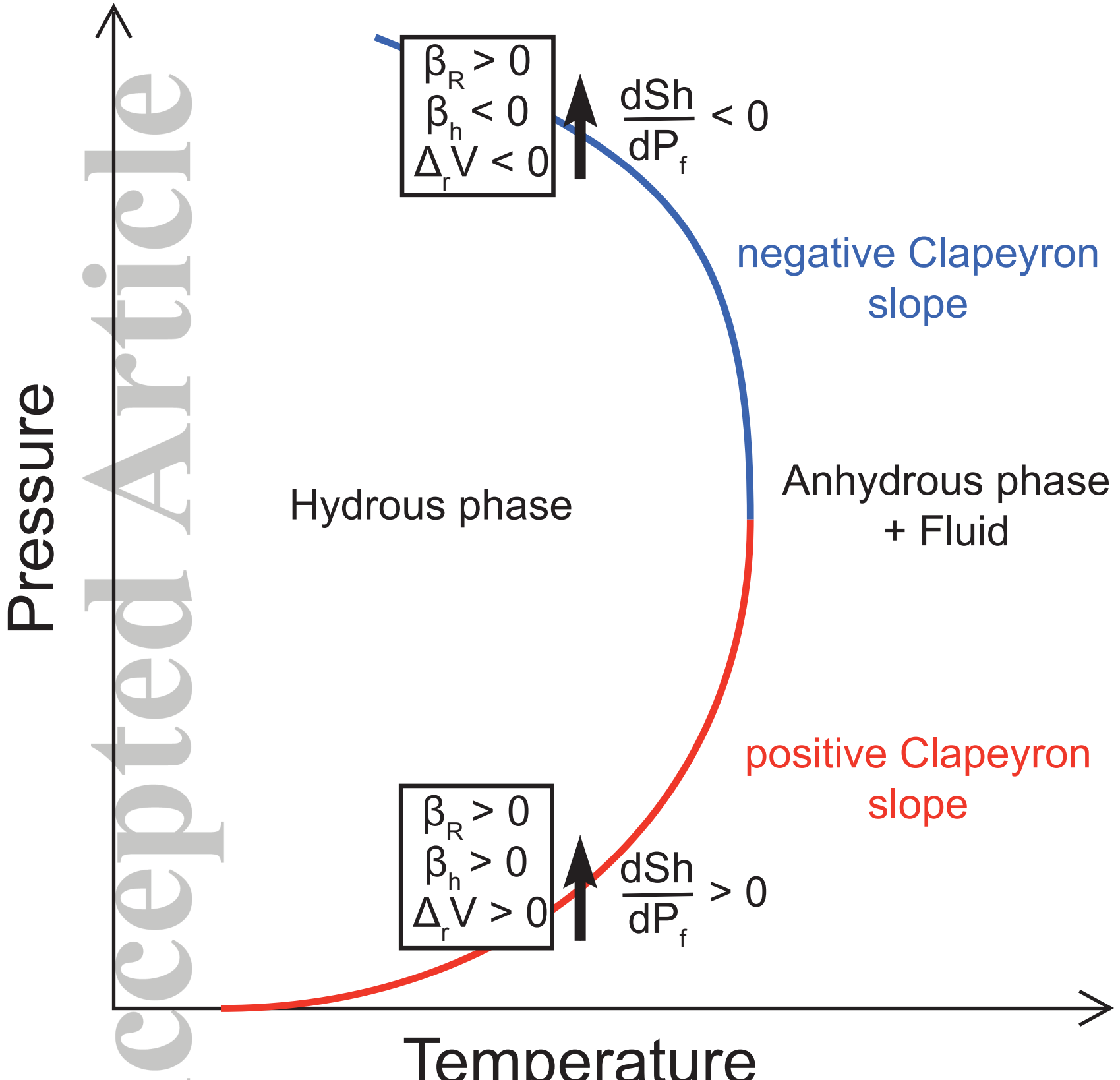

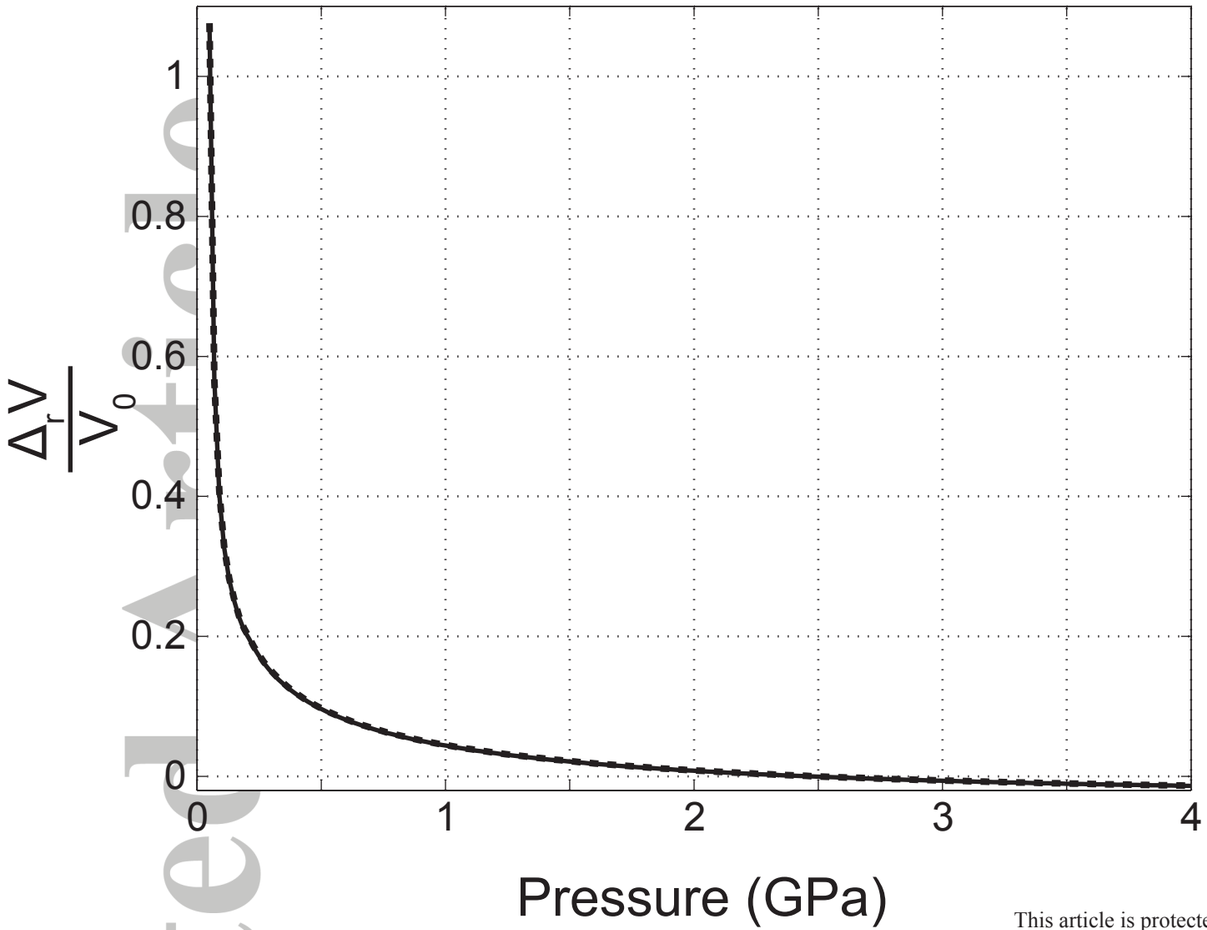

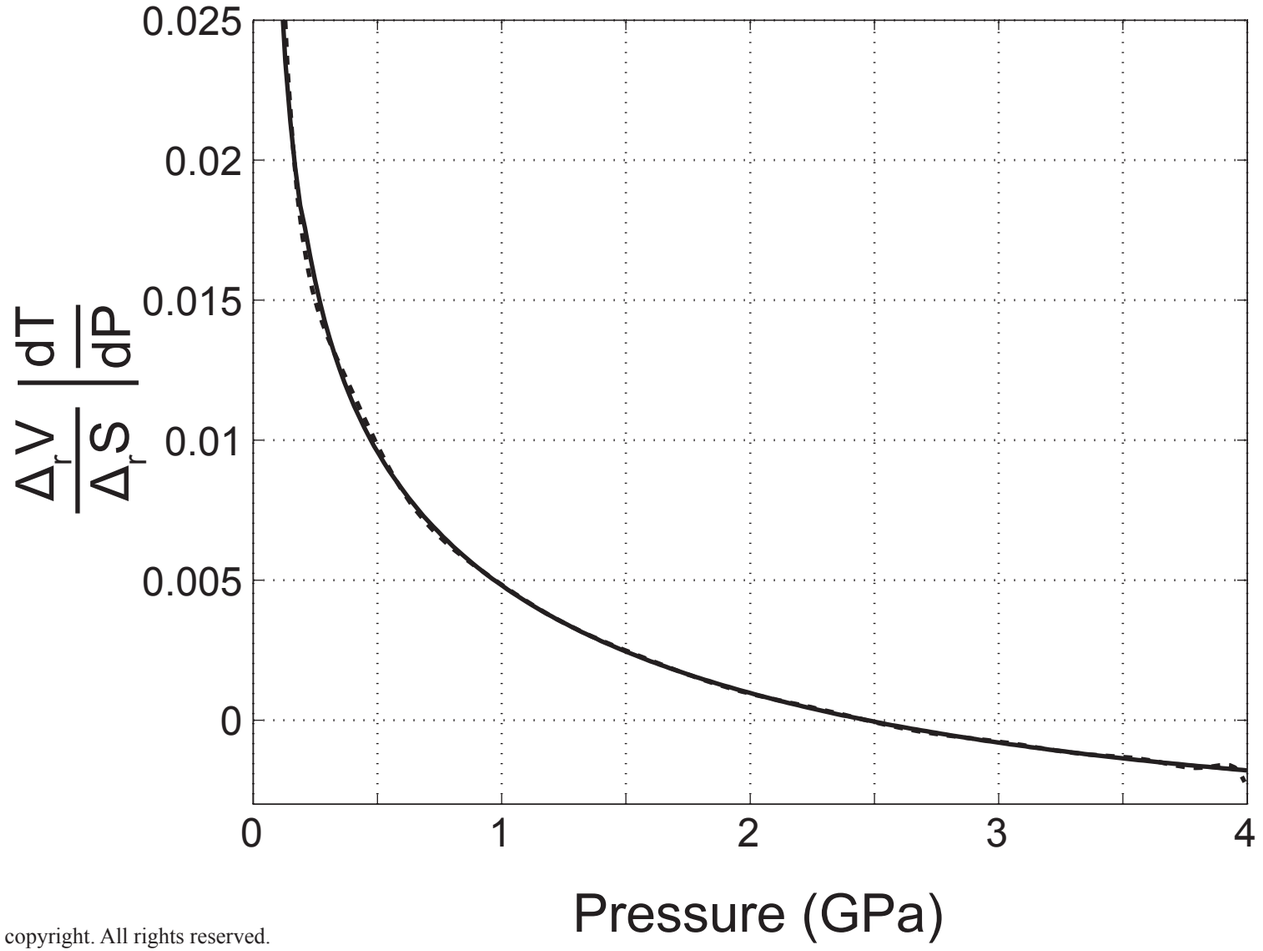

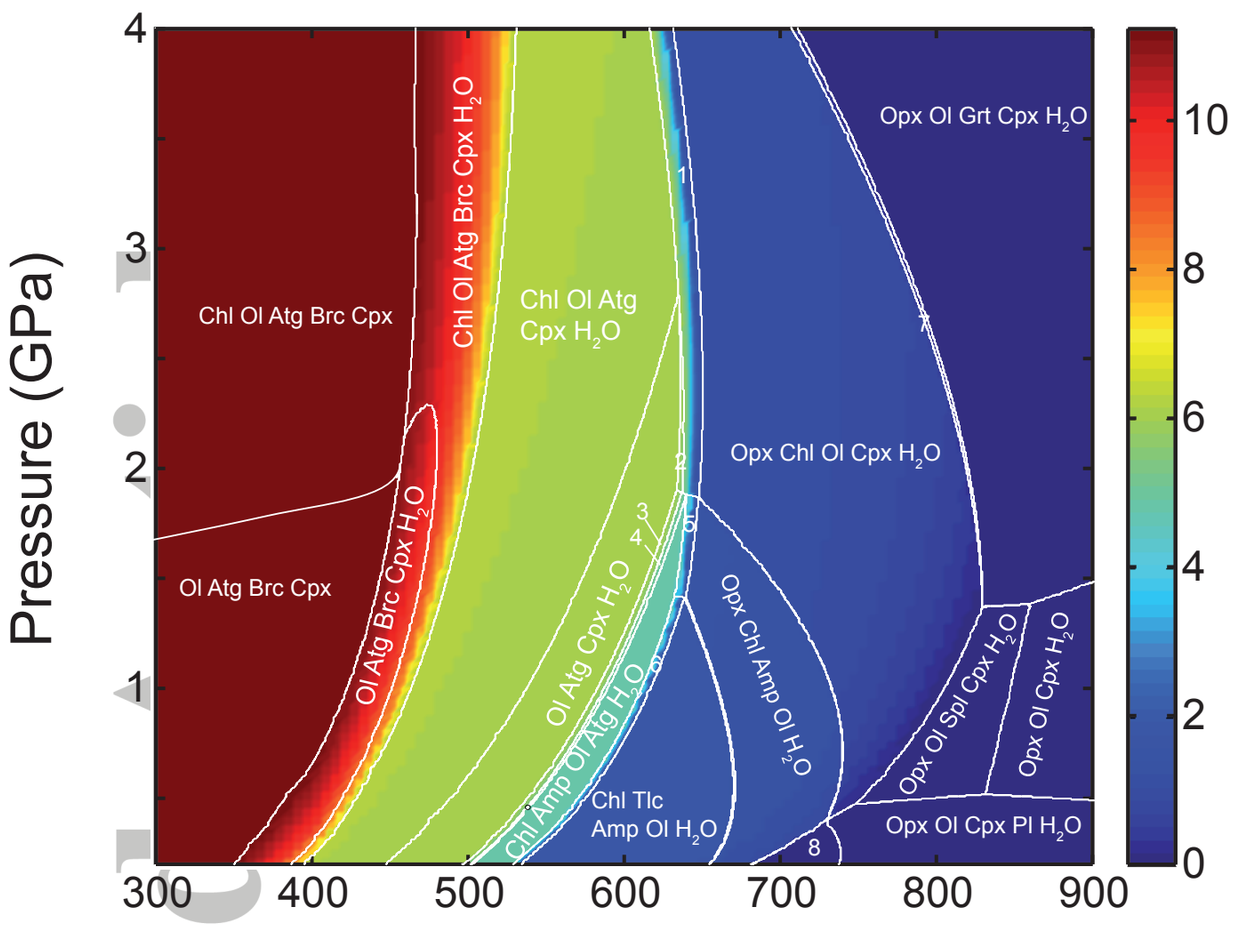

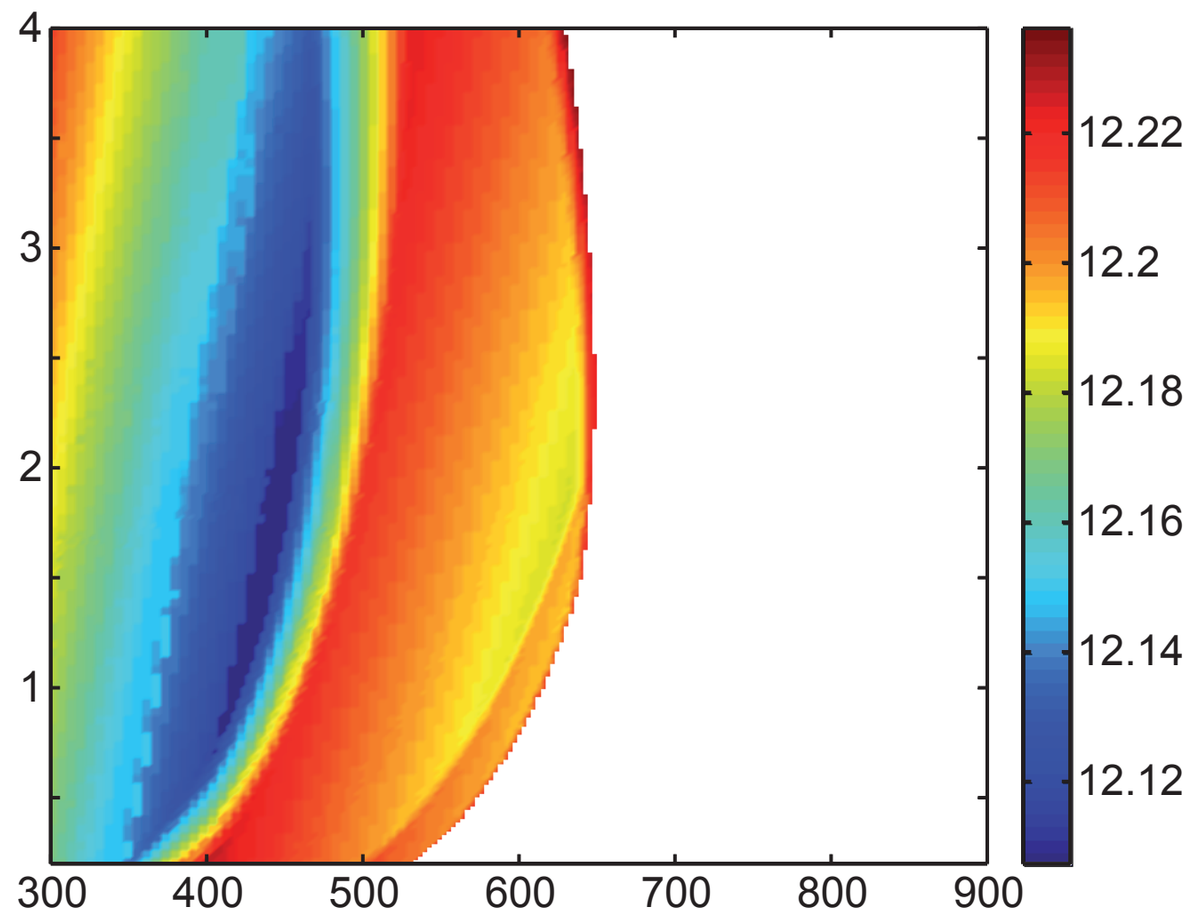

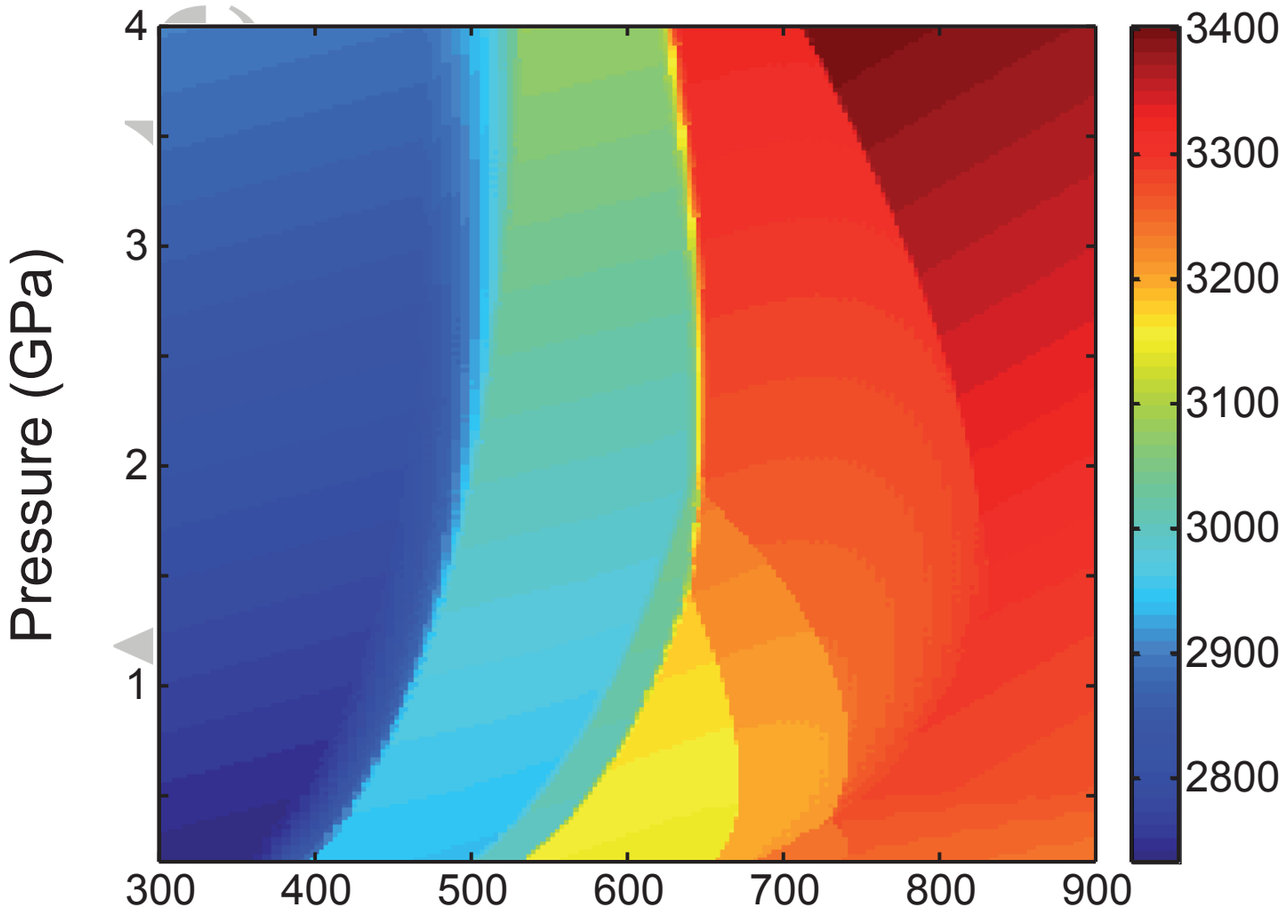

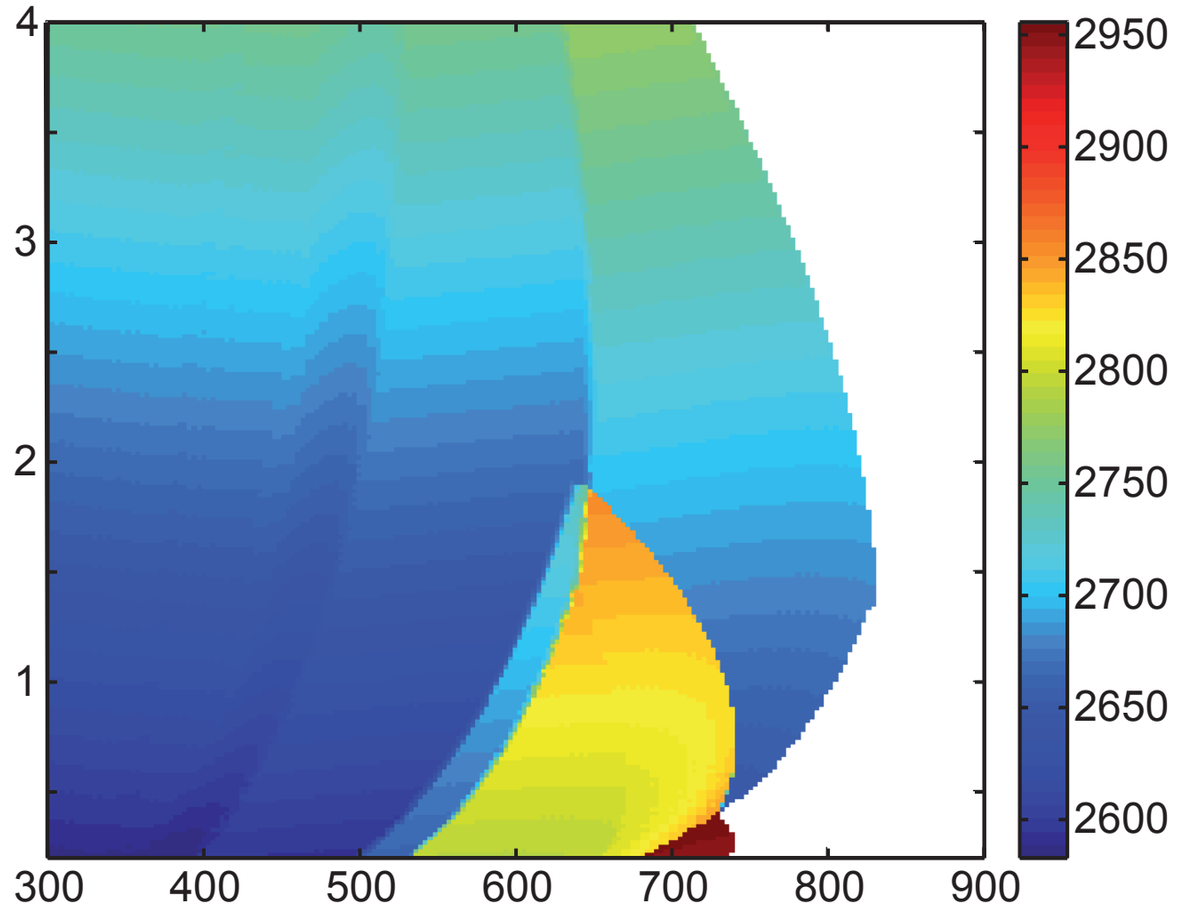

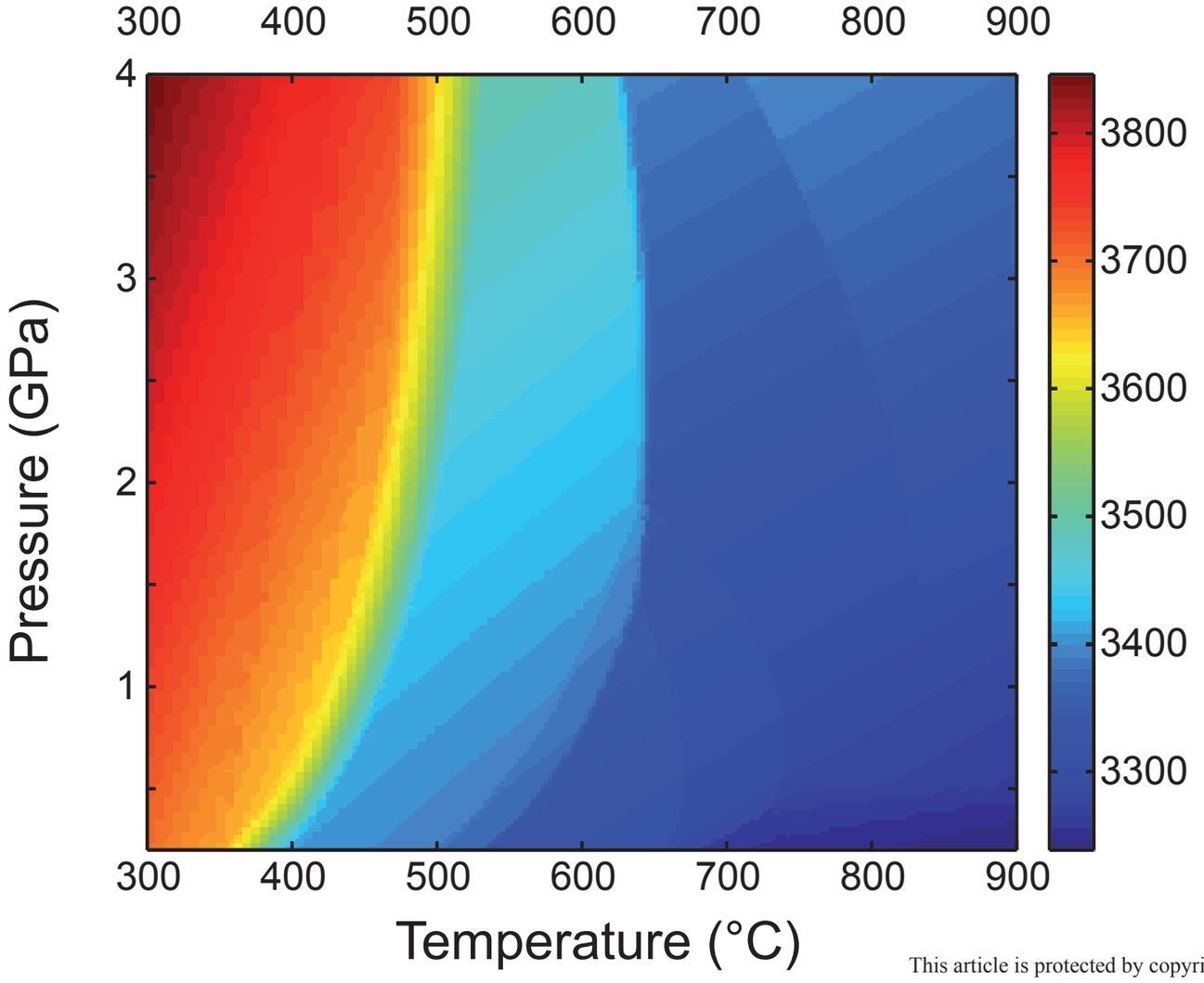

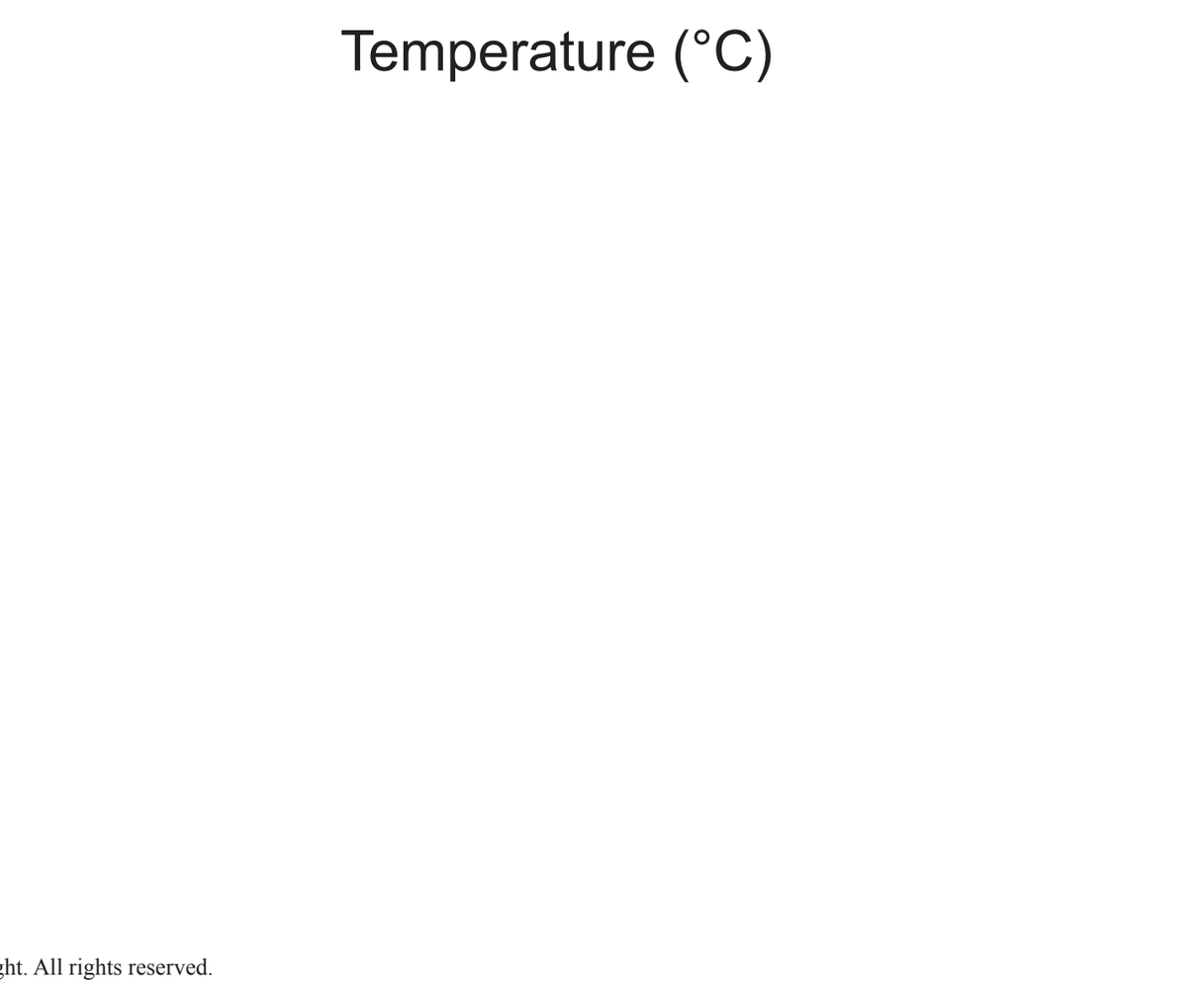

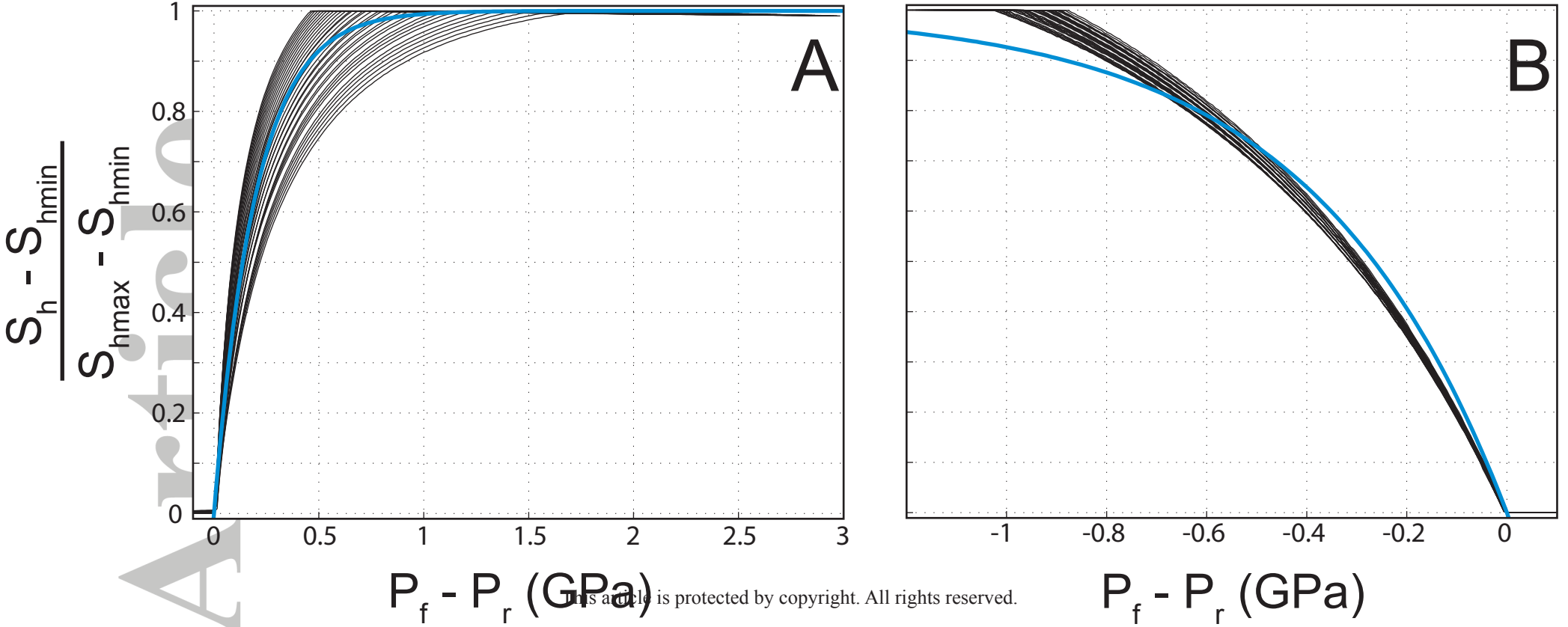

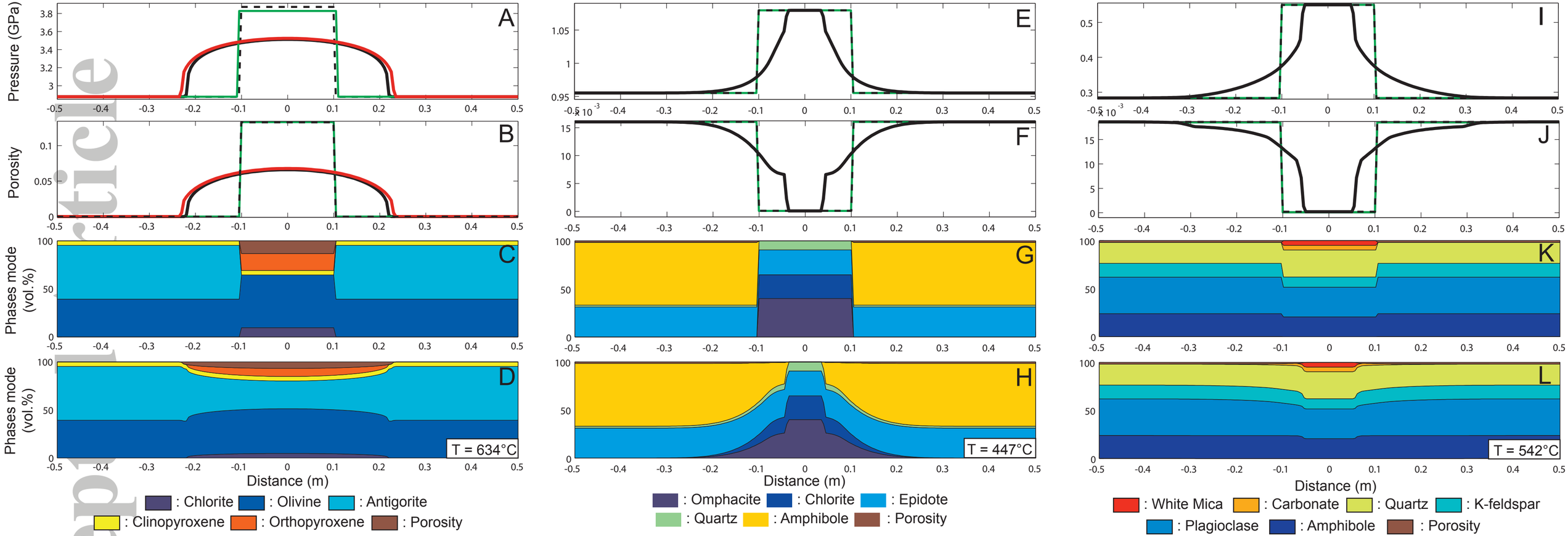

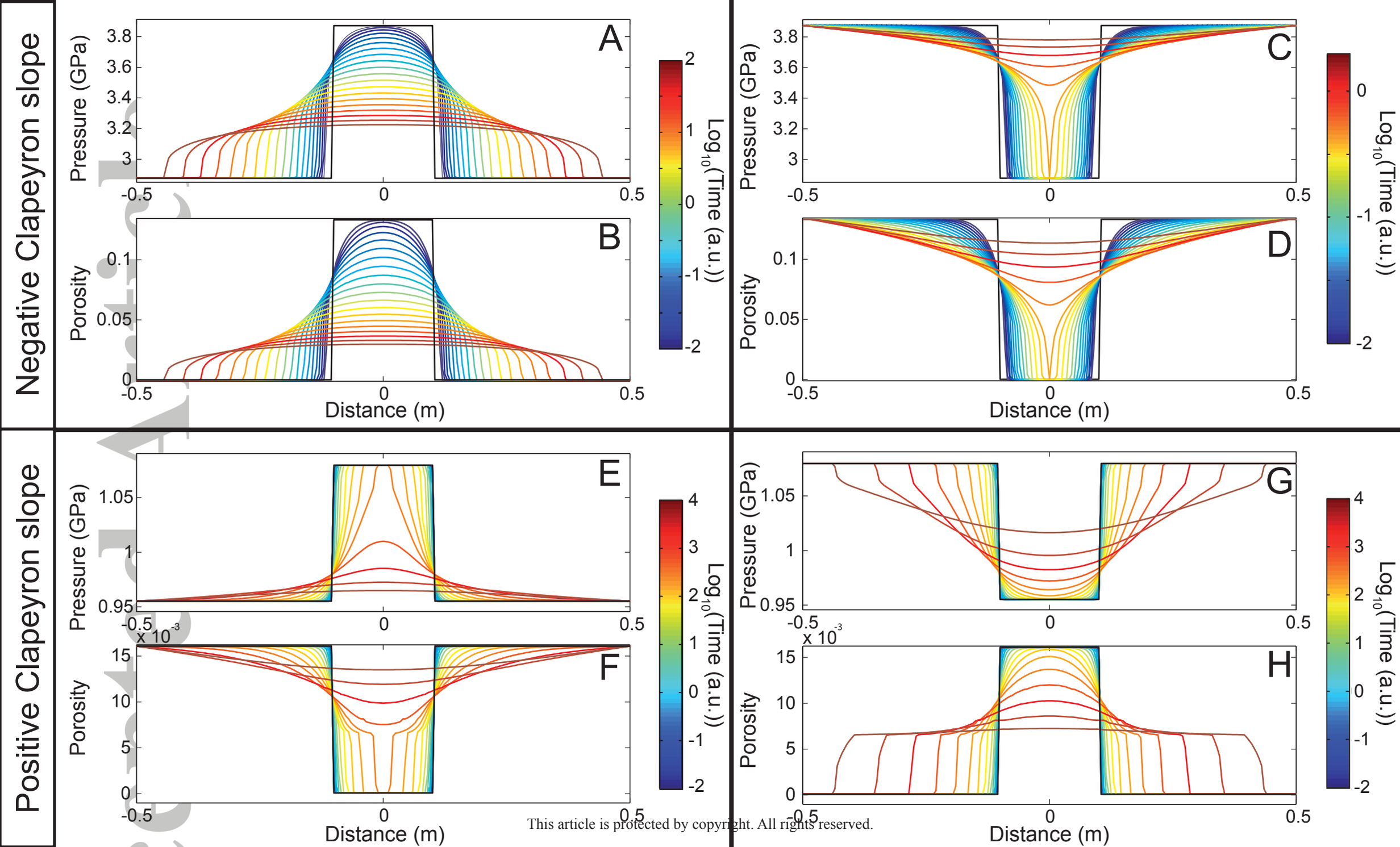

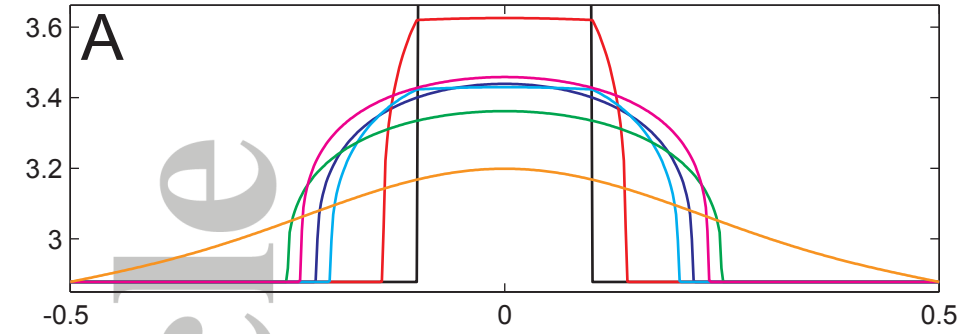

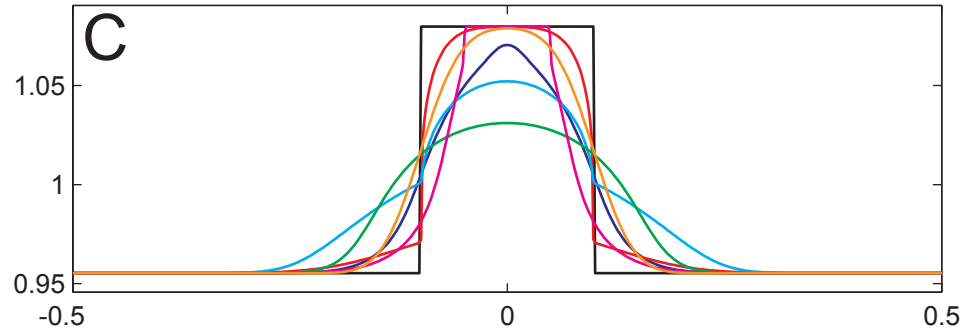

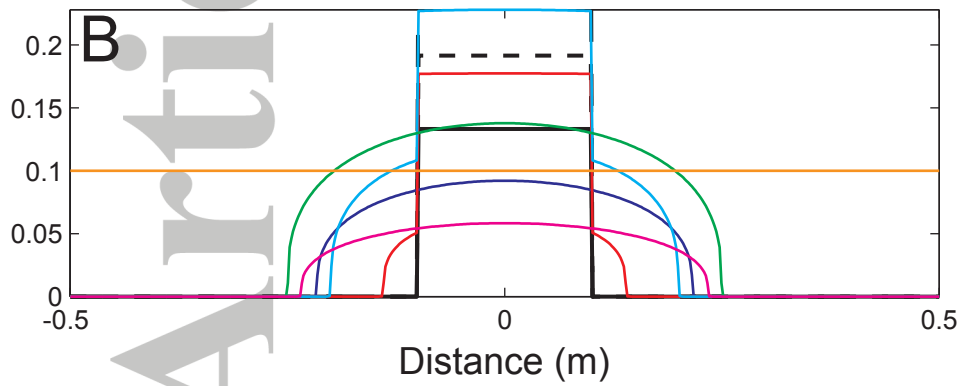

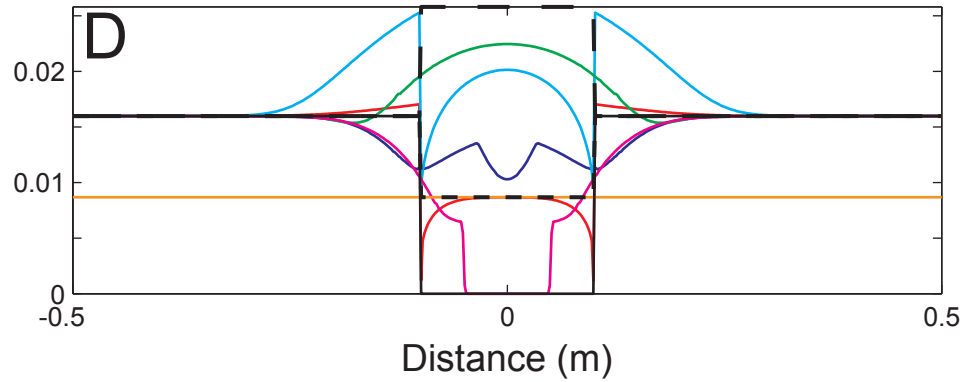

— : no reaction IC - - - : β_d- β_s'= 0.07 GPa^{-1} IC
— : no deformation — — : β_d- β_s'= 0.21 GPa^{-1} IC
— : fluid flow only
— : β_d- β_s'= 0.07 GPa^{-1}, no reaction
— : β_d- β_s'= 0.07 GPa^{-1}, reaction
— : β_d- β_s'= 0.21 GPa^{-1}, no reaction
— : β_d- β_s'= 0.21 GPa^{-1}, reaction